ChemComm

ROYAL SOCIETY OF CHEMISTRY

FEATURE ARTICLE

View Article Online
View Journal | View Issue

Cite this: *Chem. Commun.*, 2025, **61**, 7408

Supramolecular structure@MXenes for photocatalytic applications – a review

Pankaj Verma, [a] Jan H. van Maarseveen [b] and N. Raveendran Shiju *[a]

Received 16th November 2024,
Accepted 12th March 2025

DOI: 10.1039/d4cc06102k

rsc.li/chemcomm

Recently, supramolecules have emerged as innovative and eco-friendly options for photocatalytic applications due to their tunable porous structures and photophysical properties. However, their low thermal stability and chemical stability pose a significant challenge. To address this, combining supramolecules with more stable materials like MXenes, which have a low Fermi energy level, is a useful strategy, in which they can form heterostructures that enhance stability and improve photocatalytic activity. The synthesis process, whether through *in situ* or post-synthesis modifications, plays a crucial role in controlling the formation of both covalent and non-covalent interactions, as well as the morphology of the heterostructures. These interactions and the resulting morphology significantly influence the recombination and separation of charge carriers (electron–hole pairs), ultimately affecting the stability and recyclability of the heterostructures in photocatalytic applications. In this review, we discuss the importance of supramolecule/MXene heterostructures, detailing their synthesis and morphology, as well as the mechanisms involved in various applications.

1. Introduction

In the face of pressing global challenges such as fossil fuel depletion, rising energy demands, and environmental degradation, photocatalysis emerges as a promising solution.[1] This method is particularly eco-friendly because it involves the harvesting of solar energy, which is a renewable energy source, to drive chemical reactions without generating byproducts.

[a] *Catalysis Engineering Group, Van't Hoff Institute for Molecular Sciences, University of Amsterdam, Science Park 904, 1098 XH Amsterdam, The Netherlands. E-mail: n.r.shiju@uva.nl*
[b] *Synthetic Organic Chemistry Group, Van't Hoff Institute for Molecular Sciences, University of Amsterdam, Science Park 904, 1098 XH Amsterdam, The Netherlands*

Pankaj Verma

Pankaj Verma obtained her MTech and PhD degrees from Indian institute of Technology-Roorkee, specializing in nanomaterials and supramolecular chemistry, focusing on metal organic frameworks (MOFs). After that she did post-doctoral research at the Bhabha Atomic Research Centre, Mumbai, INDIA, where she worked on photocatalytic hydrogen generation via water splitting. Currently, she is working in Catalysis Engineering Group at the Van't Hoff Institute for Molecular Sciences (HIMS), University of Amsterdam, jointly advised by Dr Shiju Raveendran and Prof. Jan H. van Maarseveen. Her research focuses on heterogeneous catalysis and photocatalytic hydrogen generation using heterostructured catalytic materials.

Jan H. van Maarseveen

Jan H. van Maarseveen obtained his PhD in 1994 at the University of Nijmegen on the total synthesis of antiviral alkaloids. He then joined Solvay-Pharmaceuticals as a group leader-lead optimization. In 1999, he joined the University of Amsterdam as an assistant professor and became full professor in 2015. His research focuses on covalent scaffold-based methodology development and synthesis and applications of rotaxanes. Jan is an enthusiastic teacher and obtained several awards including the "best teacher of the year of the University of Amsterdam". In 2016, he received the Royal Dutch Chemical Society Van Marum Medal for excellence in chemistry outreach and teaching.

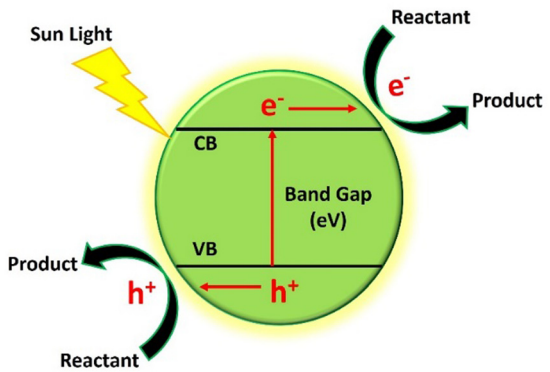

Fig. 1 Schematic representation of a photocatalytic reaction, showing electronic excitation with solar energy and the interaction of electrons and holes with the reactant molecules, leading to product formation.

This approach utilizes a semiconductor, as a photocatalyst, to absorb solar energy and generate charge carriers (electron–hole pairs)[2] (Fig. 1). These charge carriers are responsible for initiating various chemical transformations, such as hydrogen generation *via* water splitting, pollutant degradation, CO_2 reduction *etc.* The breakthrough work of Fujishima and Honda in 1972 set the foundation for photocatalysis research.[3] This work demonstrated the potential of titanium dioxide (TiO_2) photocatalysts for hydrogen generation *via* photocatalytic water splitting. Their discovery opened new avenues for researchers to produce clean hydrogen fuels from renewable sources, sparking widespread interest in developing new photocatalytic materials for various applications. Despite these advancements, the photocatalytic performance of TiO_2 is limited by many factors such as (i) a relatively wide band gap ($\sim$3.2 eV) which limits its ability for light absorption and (ii) rapid recombination of photogenerated charge carriers (electron–hole pairs), which are mainly responsible for the efficiency of photocatalytic reactions.[4]

Thus, these limitations have driven researchers to explore a wide range of other semiconductor materials with an objective of enhancing photocatalytic activity by improving the range of light absorption and minimizing charge recombination.[5] Some notable semiconductors include oxides such as SnO_2 and ZnO, as well as a variety of chalcogenide materials, such as CdSe, CdS *etc.*[6] In addition to these advanced semiconductors, researchers have also focused on next-generation materials with advanced architectures designed to enhance charge separation and improve stability, such as one-dimensional (1-D) (*e.g.*, carbon nanotubes) and two-dimensional (2-D) (*e.g.*, carbon nitrides and layered materials) materials.[7]

Recently, attention has shifted towards heterostructures, combining two or more photocatalytically active materials, such as Z-scheme systems, core–shell structures or p–n junctions. In Z-scheme systems, two photocatalysts are combined in a manner that mimics the natural photosynthesis process, enhancing charge separation and extending the range of light absorption.[8] In core–shell heterojunctions, the core material is surrounded by a shell of another photocatalytic material. This design not only enhances the charge transfer but also shields the core material from degradation, extending the lifetime of photocatalysts.[9] These heterostructures not only address the limitations of individual semiconductors but also significantly enhance photocatalytic performance. The heterostructures of supramolecules with MXenes are potential candidates in this direction.

Supramolecules, commonly known as "beyond molecules," encompass a wide range of structures formed through various non-covalent interactions, including hydrogen bonding, π–π interactions, van der Waals forces, and more.[10] Metal–organic frameworks (MOFs)[11] and covalent organic frameworks (COFs)[12] represent a distinct category of "Supramolecular Host–Guest Assemblies." In these systems, the framework serves as the host, providing space for guest molecules, such as ions or solvent molecules, to reside through weak or non-covalent interactions. In photocatalytic reactions, supramolecular materials, especially MOFs[13] and COFs,[14] have emerged as innovative, eco-friendly options and have many advantages, such as (i) high surface area and tunable pore size, providing more active sites for photocatalytic activity, (ii) high porosity enhancing reactant adsorption and diffusion,[15] (iii) tunable energy levels by selecting appropriate metal centers (in MOFs) or organic linkers (in both MOFs and COFs), enabling them to absorb in a long range, (iv) conductive linkers and π-conjugated pathways in COFs enhancing charge transport, while MOFs with appropriate metal centers acting as electron acceptors or donors,[16] and (v) possibility of post-synthetic modifications or functionalization in both MOFs and COFs.[17] However, these supramolecules often suffer from low thermal/chemical stability and rapid recombination of photogenerated electrons and holes, resulting in low photocatalytic activity with very low recyclability. Thus, combining them with more stable materials like MXenes can yield heterostructures with enhanced stability[18,19] and improved photocatalytic activity.[20]

MXenes are a class of two-dimensional (2-D) materials, known for their excellent metallic electrical conductivity, hydrophilicity similar to graphene oxide, and robust mechanical properties.[21] MXenes are typically derived from MAX phases (*e.g.*, Ti_2AlC, Ti_3AlC_2, and Ti_4AlC_3) through selective etching of

Shiju Raveendran

Shiju Raveendran leads the Catalysis Engineering Group at the University of Amsterdam. He earned his PhD from the National Chemical Laboratory-Pune, India. He then received a Royal Society (UK) postdoctoral fellowship and conducted research in the UK and USA before joining the University of Amsterdam. He is Editor-in-Chief of the Elsevier journal Sustainable Chemistry for Climate Action and serves on several editorial boards. His research focuses on the development of sustainable technologies.

aluminum, creating interlayer spaces suitable for intercalation and the formation of sandwich-like structures.[22] The presence of terminal functional groups (*e.g.*, –OH, –O, and –F) on MXene surfaces enhances their versatility, enabling the formation of hybrids with other materials such as MOFs and COFs. This makes MXenes ideal candidates for various applications due to their tunable properties.[23,24] Our group has shown the effectiveness of MXenes and MAX phases in several applications.[25–27] Although extensive research has been conducted on supramolecule/MXene composites for applications such as supercapacitors, batteries, and electro materials, there is a notable lack of comprehensive reviews focusing on their photocatalytic activity.[28] This review seeks to address this gap by summarizing the current state of research on supramolecule/MXene composites for photocatalysis (Table 1) and providing a framework for future investigations into these materials for eco-friendly applications.

2. MXenes and their optical properties

MXenes, which are carbides and nitrides of transition metals, are emerging as a new class of useful two-dimensional (2D) materials. They are renowned for their outstanding electronic conductivity and highly active metal sites with hydrophilic surfaces.[47] In 1964, Jeitschko *et al.*[48] reported the TMC phase (Zr_2TlC, Zr_2PbC, Hf_2TlC, and Hf_2PbC), which is now known as the MAX phase. Although these compounds contained thallium (Tl) in those days, note that the soluble thallium salts are highly toxic and hence it is better to avoid their use. The general empirical formula for the MAX phase is $M_{n+1}AX_n$, where M denotes a transition metal, such as titanium (Ti), scandium (Sc), niobium (Nb), molybdenum (Mo), tantalum (Ta), or vanadium (V); A represents a group 13 (boron family) or group 14 (carbon family) element; and X is carbon (C) and/or nitrogen (N). In the MAX phase, the M–A bond, which is a chemically active metallic bond, can be easily broken using a selective chemical etching method, resulting in MXenes.[49] In the simplest way, MXenes can be divided into three parts: (1) an intramolecular region composed of alternative arrangement of titanium (Ti) and carbon (C) *via* the formation of an ionic bond. This is the main skeleton structure. (2) The interlayer region formed by non-covalent interactions, such as hydrogen bonding or van der Waals forces, between the layered structures; and (3) the surface terminated functional groups.[50,51] Depending on the etching agents used, MXenes have different terminal functional groups (T_x), such as –O, –F, –OH, *etc.* A schematic representation of possible MXene structures (M_2XT_x, $M_3X_2T_x$, $M_4X_3T_x$, and $M_5X_4T_x$) is shown in Fig. 2. Similar to their corresponding MAX phases, MXenes have a hexagonal close-packed structure, in which the octahedral voids are occupied by X atoms.[21,52]

To date, various methods have been documented for the preparation of MXenes from their corresponding MAX phases. Synthesizing high-quality MXenes is challenging, and the process is influenced by many factors, such as reaction conditions, the type of etching agent, the type of MAX precursor, and others. The most popular synthesis method is etching, which utilizes various chemicals and bio-materials such as hydrofluoric acid, alkalis, Lewis acidic salts, and algae extracts, as well as electrochemical processes and photolithography.[53] The selection of the etching method used primarily depends on the type of A-group element, the transition metals, and the bonding between them.[54] According to the literature, acid etching is beneficial for MAX phases containing Al and Si as A-group elements, whereas MAX phases containing Al, Si, Zn, and Ga as A-group elements can be easily converted into MXene nanosheets using molten salt etching methods. Additionally, the exfoliation of nanosheets also depends on the strength of bonding between transition metals and A-group elements.[55] In the periodic table, the reactivity of transition metals decreases from left to right. Therefore, more stringent conditions are necessary for MAX phases containing transition metals such as Cr, Mo, and W, in contrast to those with Ti, Zr, and Hf.[56]

The optical properties mainly depend on the structural and electronic properties of materials. In MXenes, the presence of terminal functional groups and chemical composition significantly affect the optical properties. Lashgari *et al.*[57] demonstrated through DFT calculations that without terminal functional groups (T_x), pristine MXenes exhibit metallic character due to the overlapping of the conduction band (CB) and valence bands (VB) at the Fermi level. During the course of synthesis, the outermost metallic layer in MXenes is terminated by terminal functional groups. Further DFT studies predicted that the optical properties are mainly dependent on the type as well as the orientation of terminal functional groups, irrespective of the composition of MXenes. Berdiyorov[58] employed DFT calculations to reveal the role of terminal functional groups (such as −F, −O, and −OH) in the electronic structure of $Ti_3C_2T_2$ MXenes. In the visible range, fluoride (–F) and hydroxy (–OH) groups exhibited lower absorption and reflectivity compared to bare MXenes. In contrast, the surface with an –O terminal functional group showed enhanced absorption and reflectivity. In the ultra-violet (UV) range, surface functionalization showed a positive impact on improving the anti-ultraviolet properties of MXenes.

3. MOFs and their electronic properties

MOFs, a subset of porous frameworks, are widely recognized as inorganic–organic hybrid materials. They are prepared from inorganic nodes and organic linkers.[59] The inorganic nodes are metal centers (mainly transition or lanthanide metals) or metal oxide clusters, known as secondary building units (SBUs), whereas organic linkers consist of functional groups or anions[60] such as carboxylates, phosphonates, sulfonates *etc.* The geometry of MOFs mainly depends on the coordination number and geometry of the central metal ion, and also the nature of functional groups, such as monodentate, bidentate or multidentate (Fig. 3(a)).[61] In principle, a bridging linker reacts with a metal ion that has more than one vacant or labile site, resulting in the formation of frameworks with different topologies.

Table 1 Summary of supramolecule (MOF or COF)/MXene-based catalysts for different photocatalytic applications reported in previous literature studies

S. N.	Photocatalyst	Preparation method	Structure	BET surface area ($m^2\ g^{-1}$)	Light source/ range	Other conditions	Photocatalytic activity	Result	Recyclability	Ref.
1.	TU series (Ti_3C_2/UiO-66-NH_2)	One-pot hydrothermal method	Irregular cubic-spherical morphology of UiO-66-NH_2 was decorated with Ti_3C_2 nanosheets	984	Simulated solar irradiation	Sacrificial reagent (0.1 M Na_2S and 0.1 M Na_2SO_3)	Hydrogen production	204 μmol $h^{-1}\ g^{-1}$	3 runs	29
2.	Ti_3C_2/TiO_2/ UiO-66-NH_2	Electrostatic adsorption *via* one-step hydrothermal method	Uniform attachment of UiO-66-NH_2 on the surface of TCA with more exposed reactive sites	987.5	Simulated solar irradiation ($350 < \lambda < 780$ nm)	Sacrificial reagent 0.1 M Na_2S and 0.1 M Na_2SO_3	Hydrogen production	1980 μmol $h^{-1}\ g^{-1}$	3 runs	30
3.	TCs/Cu-PMOF	One-step solvothermal process	Both TCs and Cu-PMOF had 2D lamellar structures while 2D sheets' structure was observed in the image of the TCs/Cu-PMOF heterostructure	20.3	300 W Xe lamp (340–780 nm)	Sacrificial reagent triethanolamine	Hydrogen production	10.15 mmol g^{-1}	5 runs	31
4.	TT/CuTMOF nanocomposite	Cu^{2+} is introduced into Ti_3C_2@TiO_2 (TT) to provide sites for the *in situ* assembly of the Cu-TCPP MOF	TT/CuTMOF showed thin sheet-like structures with close interfacial contact	—	Simulated solar irradiation ($340 < \lambda < 780$ nm)	Sacrificial reagent triethanolamine (TEOA)	Hydrogen production	19.06 mmol g^{-1}	5 runs	32
5.	Ti_3C_2@MIL-NH_2	*In situ* hydrothermal growth method	Irregular nanoparticles of MOFs were *in situ* grown on the accordion like layered MXene structure	69.2	Simulated solar irradiation	Sacrificial reagent 20 mL CH_3OH with 0.3 mL TEOA	Hydrogen production	4383.1 mmol g^{-1}	4 runs	33
6.	Ti-MOF/QDs/ ZIS	Electrostatic attraction method	$ZnIn_2S_4$ nanosheets covering the surface of the Ti-MOF crystals and 2D Ti_3C_2 MXene lamellae stacks	179.8	$\lambda > 420$ nm	Sacrificial reagent 0.35 M Na_2S and 0.25 M Na_2SO_3)	Hydrogen production	2931.9 μmol $g^{-1}\ h^{-1}$	4 runs	34
7.	ATNT	*In situ* growth of β-ketoenamine-linked COFs onto NH_2—$Ti_3C_2T_x$ MXenes *via* covalent connection	COF sticks with a sheet-like microstructure are uniformly attached on NH_2–$Ti_3C_2T_x$	683.6	$\lambda > 420$ nm	Sacrificial reagent L-ascorbic acid	Hydrogen production	14.20 mmol g^{-1}	6 runs	35
8.	MXene/MOF (MXOF)	*In situ* synthesis of MOFs in the presence of MXene nanosheets	MOF particles with spherical shapes on the MXene nanosheet surface	37.69	Visible-light irradiation (mercury vapor (250 W))	Time required (60 min)	Photodegradation of DR31 (azo dye) and MB (thiazine dye)	62% of MB and 35% of DR31 dyes	4 runs	36
9.	Sn–Bi–MOF/ Ti_3C_2	*In situ* solvothermal method	Sn–Bi–MOF nanoparticles were inserted into the layered structure of Ti_3C_2	145.8	500 W xenon lamp	Time required (90 min)	Photocatalytic degradation of tetracycline (TC)	96.2% degradation efficiency of TC	4 runs	37
10.	MIL-88A(Fe)/ MXene (D-MIL-88A(Fe), W-MIL-88A(Fe), S-MIL-88A(Fe))	Hydrothermal *in situ* growth	Many small fine grain particles of MIL-88A(Fe) on the smooth Ti_3C_2 MXene surface.	12.4	Xenon lamp	Time required (10 min)	Degradation of common pollutants in wastewater	70% degradation of sulfamethoxazole by DA-M100	3 runs	38
11.	NH_2-MIL-125(Ti)(TiO_2)/ Ti_3C_2	One-step solvothermal strategy	MT0 – plate-like nanosheet morphology, MT0.1 – rod-like nanoparticles, MT1 – enlarged particles with the surface uniformly coated by TiO_2 nanosheets, MT5 – enlarged particles with the surface uniformly coated by TiO_2 nanoparticles	329	$\lambda > 420$ nm	Time required (60 min)	Photocatalytic degradation of tetracycline hydrochloride (TC-HCl)	82.80% degradation of tetracycline over MT5	4 runs	39

Table 1 (*continued*)

S. N.	Photocatalyst	Preparation method	Structure	BET surface area ($m^2\ g^{-1}$)	Light source/ range	Other conditions	Photocatalytic activity	Result	Recyclability	Ref.
12.	TP-COFs/ $Ti_3C_2T_x$ (TCM)	*In situ* growth of COFs over MXenes	TC nanofibers (about 500–1500 nm in length) attach in an orderly fashion on the layered NH_2–$Ti_3C_2T_x$, forming a lawn-like TCM composite	—	300 W xe lamp and equipped with an ultra-violet cutoff filter (λ > 420 nm)	Electron donor (15% w/v TEOA)	CO_2 reduction	Formate yield – 11.9 & 2.7 mmol L^{-1} (with & without an electron mediator, respectively)	—	40
13.	ZT-450	ZIF-67 was *in situ* grown on $Ti_3C_2T_x$ MXene	Spreading of polyhedral ZIF-67 on the $Ti_3C_2T_x$ MXene surface	62.6	Xe lamp (420–780)	—	CO_2 reduction	Yields – CO (62.7 μmol g^{-1}), CH_4 (6.7 μmol g^{-1}) and H_2 (7.3 μmol g^{-1})	4 runs	41
14.	pink/TC/SBM	A simple electro-static self-assembly method	2D structure of pine and SBM rapped around TC and all three are con-nected with electrostatic connections	—	300 W he lamp (simulated sunlight)	Electron donor (20 ml TEOA)	CO_2 reduction	Yields – CO (36.33 μmol g^{-1} h^{-1})	4 runs	42
15.	Co–Co LDH/ TNS	*In situ* MOF derived solvothermal method	LDH nanosheets staggered and standing on a TNS substrate to form a nanoarray structure	—	5 W LED lamp (400–1000 nm)	Electron donor (1 ml TEOA)	CO_2 reduction	Yields – CO (1.25×10^4 μmol g^{-1} h^{-1})	5 runs	43
16.	Ti_3C_2/TpPa-1/ Cu_2O	*In situ* growth of a TpPa-COF on MXene through the Schiff base reaction, followed by NP anchoring	Cu_2O spherical nanoparticles grew on the accordion like structure of Ti_3C_2/ TpPa-1	—	—	Method – plate colony counting method	Antibacterial activity	High antibacterial prop-erties against *P. aerugi-nosa* and *S. aureus*, with antibacterial rates of 99.62% and 98.90%, respectively	3 runs	44
17.	Ti_3C_2/TpPa-1/ Ag	Covalently con-nected Ti_3C_2/TpPa-1 through the Schiff base reaction, anchored by Ag NPs	Ag nanoparticles were highly dis-persed on the surface of Ti_3C_2/TpPa-1	—	—	Method – plate colony counting method	Antibacterial activity	Antibacterial activity against *P. aeruginosa* and *S. aureus*, with anti-bacterial rates of 99.60% and 99.78%, respectively	3 runs	45
18.	Cu-TCPP/Ti_3C_2	*In situ* self-assembly method	Sheet-like structure	—	—	Method – spread plate method	Antibacterial activity	Antibacterial activity against *S. aureus*, with antibacterial rates of 99.73%	—	46

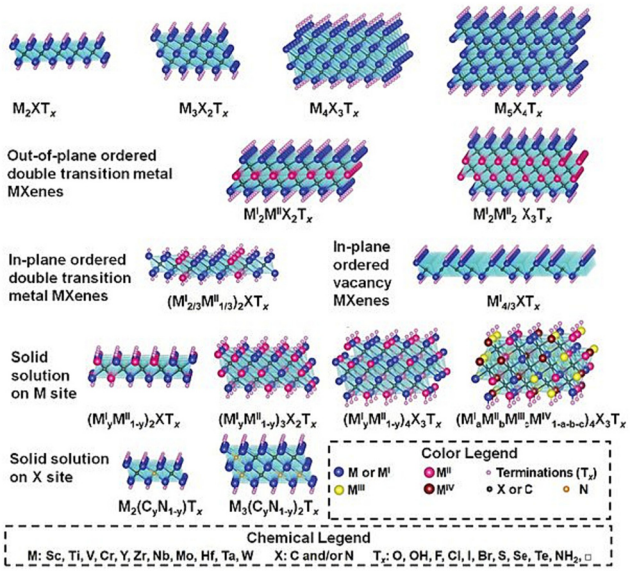

Fig. 2 Representation of the structure and compositions of MXenes. Reprinted with permission from ref. 21; Copyright 2021 Wiley-VCH GmbH.

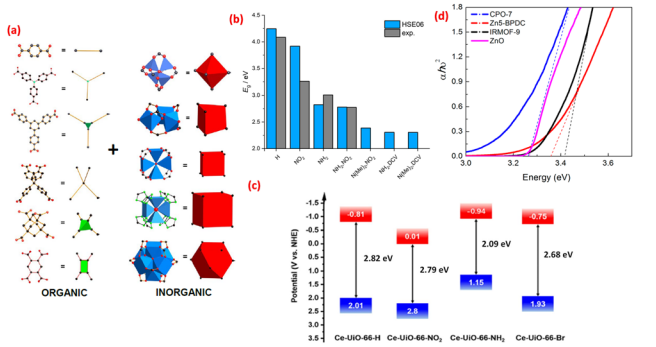

Fig. 3 (a) Basic topological diagrams for 1D, 2D and 3D MOFs (reprinted with permission from ref. 61. Copyright 2012 American Chemical Society). (b) Comparison of calculated and experimental band gaps in functionalized ligands (reprinted from open access under Creative Commons CC BY 3.0 from ref. 62). (c) Band energy structure of UiO-66(Ce)-X (reprinted with permission from ref. 63) Copyright 2019 WILEY-VCH Verlag GmbH & Co. KGaA, Weinheim. (d) Optical band gap energy of a Zn-based MOF (reprinted with permission from ref. 64). Copyright 2012 American Chemical Society.

In MOFs, the electronic properties (band gap shifting) can be achieved by (i) exchanging ligands with more conjugated ligand systems,[65] (ii) generating vacancies and defects in the system,[66–69] (iii) altering the shape of MOFs at the nanoscale[70,71] and (iv) functionalization of organic linkers (such as $-NH_2$, $-NO_2$, –OH, –Me *etc.*) leading to a band shift by donating a 2p electron to the aromatic linker.[72] For example, MIL-125, synthesized from the 4-benzenedicarboxylate (bdc) linker, has a band gap in the UV region (3.6 eV, 345 nm)[73] whereas MIL-125-NH_2, synthesized from a mono-aminated bdc-NH_2 linker, has a band gap in the visible region (2.6 eV, 475 nm).[74] Treger *et al.*[62] performed a DFT study on the effect of electron-donating and/or electron-withdrawing functional groups on the optical properties of MOFs by introducing functional groups into the ligand (terephthalic acid) of UiO-66 MOFs (2.96 eV). These ligands contain amine ($-NH_2$) or dimethylamine ($-NMe_2$) as an electron donating group and a nitro ($-NO_2$) or dicyanovinyl (DCV) group as an electron withdrawing group. Generally, the introduction of functional groups in UiO-66 MOFs decreases the band gap but the extent of the effect is based on the electron donating/withdrawing nature of the group. The electron-donating functional group lowers the band gap more significantly compared to electron-withdrawing groups (Fig. 3(b)).[62] In the case of the $-NH_2$ group, a new band gap state is generated over the valence band maximum (VBM) due to the presence of free electron pairs of nitrogen atoms (UiO-66-NH_2, 2.75 eV). In contrast, introduction of $-NO_2$ groups showed only a small decrease in the band gap due to strongly bound electrons which formed a localized state (UiO-66-NO_2, 2.93 eV).

The functionalization of ligands in MOFs not only decreases the band gap but also alters the alignment of the VB and CB.[70] For example, $-NH_2$ functionalization increases the reduction potential of UiO-66(Ce)-NH_2 by shifting the CB band (LUMO) to more negative values, whereas $-NO_2$ groups shift the VB (HOMO) position to more positive values relative to the non-functionalized UiO-66(Ce) with respect to the NHE (Fig. 3(c)).[63,70] For photocatalytic overall water splitting (OWS), the HOMO (VB edge) and LUMO (CB edge) must align with the thermodynamic potentials of the hydrogen evolution reaction (HER) and oxygen evolution reaction (OER). The energy difference (band gap) between the HOMO (VB edge, approximately −0.41 V *vs.* NHE) and LUMO (CB edge, approximately 0.82 V *vs.* NHE) should fall within the range of 1.8–2.4 eV.[75] For example, utilizing terephthalate-based mixed ligands with $-NH_2$ substituents (HOMO approximately −0.94 V *vs.* NHE, LUMO approximately 1.15 V *vs.* NHE, band gap 2.09 eV) and/or −Br substituents (HOMO approximately −0.75 V *vs.* NHE, LUMO approximately 1.93 V *vs.* NHE, band gap 2.68 eV) offers a promising approach to synthesize functionalized UiO-66(Ce) with the desired band gap energy and band alignment.[63]

Additionally, the incorporation of a halogen atom into an aromatic system can also reduce the band gap. The combined effect of two factors—the electron-donating effect (+C effect, conjugative effect) and the electron-withdrawing effect (−I effect, inductive effect)—contributes to an increase in the

Table 2 Some of the reported band gaps in different MOFs

MOFs	Band gap (eV)	Ref.
MIL-125	3.6	73
MIL-125-NH2	2.6	74
UiO-66	2.91	62
UiO-66-NH_2	2.78	62
IRMOF-2F	3.20	76
IRMOF-2Cl	3.09	76
IRMOF-2Br	2.96	76
IRMOF-2I	2.65	76
IRMOF-20C	0.95	76
IRMOF-20O	2.65	76
IRMOF-20S	2.52	76
IRMOF-F4	2.77	76
IRMOF-1	3.46	76
Zn5-BPDC	3.36	64
CPO-7	3.26	64
IRMOF-9	3.42	64

HOMO energy level.[76] Thus, among all halogens, iodine is the best candidate for reducing the band gap and increasing the valence band maximum (VBM) (Table 2). In addition to the above, the size and type of metal centres and/or SBUs also affect the electronic properties of MOFs (Fig. 3(d)).[64] These modifications not only change the electronic properties of MOFs but also open new avenues for exploring MOFs as new semiconductors.[77]

4. COFs and their optical properties

COFs, another subclass of porous crystalline materials, are formed by covalent bonds between two or more organic building blocks. These building blocks range from small organic molecules to macromolecules such as polymers[78] (Fig. 4). The high stability of COFs mainly depends on the strength of covalent bonds formed between the building blocks such as C–N, C–C, and C–O bonds. For the first time in 2005, Yaghi *et al.*[79] introduced COFs, formed by the condensation reaction of organic building blocks. In contrast to MOFs, COFs are formed solely through covalent bonds between light elements such as hydrogen, boron, carbon, nitrogen, and oxygen, without the involvement of heavy metal atoms. MOF frameworks are created through co-ordination bonds formed between metal centers and organic ligands, whereas COFs are characterized by formation of covalent bonds, providing them high stability.[80] Generally, COFs have low densities with exceptional stability under harsh conditions, such as acidic, basic, oxidative, and reductive conditions.

The optical properties of COFs mainly depend upon the type of framework, topology, chemical composition, presence of functional groups, specific surface area and porosity. The presence of chromophores such as aromatic rings or extended conjugated systems enhances the photophysical properties of COFs in visible or UV-visible ranges. The type of covalent bonding formed during synthesis, such as imine linkages, triazine-based linkages, and β-ketoenamine linkages, and the presence of functional groups, such as $-NO_2$, $-NH_2$ *etc.*, can also alter the electron density and photophysical properties (Table 3). In a critical review, Wang *et al.*[81] clearly explained that the structure of frameworks, from the 0-dimensional structure to the 3-dimensional structure, and the intact weak

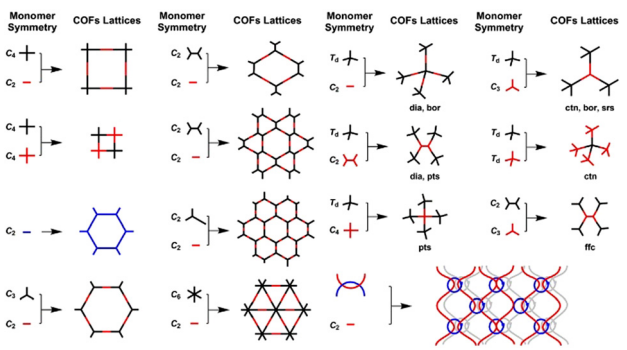

Fig. 4 Basic topological diagrams of COFs. Reprinted with permission from ref. 78. Copyright 2020 American Chemical Society.

Table 3 Some of the reported band gaps in different COFs

COFs	Band gap (eV)	Ref.
TP-DTP	2.42	83
TP-EDDA	2.34	83
TP-BDDA	2.31	83
COF-OH-0	2.68	84
COF-OH-1	1.90	84
COF-OH-2	2.02	84
COF-OH-3	2.28	84
TpPa-H	1.56	85
Tp-BD	1.64	85
Tp-DTP	1.83	85
TpPa-Cl2	1.58	85
DHBQ-TAPP-COF	1.09	86
COF_{D4}	2.30	87
COF_{D19}	2.33	87
Am-COF_{D4}	2.20	87
Am-COF_{D19}	2.14	87

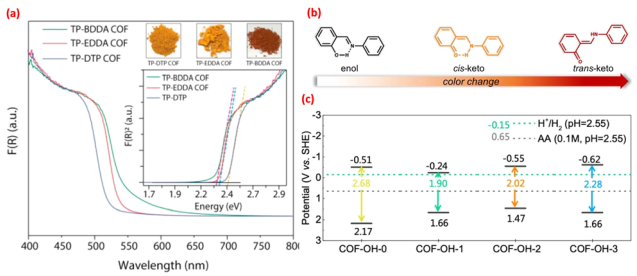

Fig. 5 (a) UV-Vis DRS of COFs showing the calculation of the band gaps as well as the optical images of COF powders (reprinted with permission from ref. 83). Copyright 2017 American Chemical Society; (b) color change due to proton tautomerism; (c) band position and bandgap of COFs (b & c reprinted with permission from ref. 84. Copyright 2022 Royal Society of Chemistry).

bonding such as H-bonding, π–π interactions *etc.* between layers, directly influence the separation and transfer of electron–hole pairs through the frameworks. Li *et al.*[82] demonstrated that the presence of donor–acceptor (D–A) groups and increased conjugated systems that participated in COFs results in a narrower optical band gap. Pachfule *et al.*[83] synthesized β-ketoenamine based COFs functionalized with phenyl, acetylene and diacetylene, named TP-DPT, TP-EDDA and TP-BDDA COFs respectively, for photocatalytic hydrogen generation *via* water splitting. A comparison of their optical properties revealed a notable reduction in the band gap by the introduction of a diacetylene group. Specifically, TP-BDDA exhibited a small band gap (2.31 eV), in comparison to TP-EDDA (2.34 eV) and TP-DTP (2.42 eV) (Fig. 5(a)). Chen *et al.*[84] investigated the impact of proton tautomerism (Fig. 5(b)) on the optical properties of COFs, named COF-OH-*n* (where *n* = 0–3 denotes the number of –OH groups), formed by β-ketoenamine linkages. COF-OH-0, with a band gap of 2.68 eV, exhibited the narrowest absorption spectrum due to the absence of –OH groups. In contrast, COF-OH-1, COF-OH-2 and COF-OH-3 displayed progressively broader absorption spectra with band gaps of 1.90, 2.02 and 2.28 eV, respectively (Fig. 5(c)).

5. Synthesis methods

Supramolecules, MOFs and COFs, are significant branches of porous polymeric materials with tunable structures, either in terms of porosity or functionality of frameworks. MOFs are synthesized from metal centers coordinated with multi-functional ligand systems whereas COFs are organic polymers formed through the creation of covalent bonds between organic moieties.[88] The presence of organic ligands with functional groups makes these materials ideal precursors for the conversion to other carbon based materials.[89]

In air and water environments, the metastable metal atoms present on the surface of MXenes can transform into stable metal oxides through a spontaneous reaction with oxygen-containing groups.[90,91] To enhance the stability and photophysical properties, MXenes are often used to form composites with supramolecules and their derivatives.[92] Thus, for the synthesis of MXene based composites with supramolecules, many strategies have been employed which can be classified into two categories an *in situ* method and post-synthetic modification (Fig. 6).

5.1 *In situ* method

In this method, composite formation occurs in a single step, enabling the components to bond through the available active sites. A large number of interactions are formed between the components during the growth of the framework. Typically, the process of supramolecule/MXene heterostructure formation involves mixing MXenes with the building blocks of supramolecular frameworks under controlled synthesis conditions[93] (Fig. 6). In the case of MOFs, the building blocks are deprotonated ligands and metal ions. Qu *et al.*[52] synthesized Ni-MOF/$Ti_3C_2T_x$ hybrids by adding MXenes to the solution containing nickel salt followed by the addition of terephthalic acid as a ligand, with stirring at room temperature. Similarly, Wen *et al.*[94] synthesized a bimetallic CoNi-ZIF-67/$Ti_3C_2T_x$ composite by adding MXenes to the solution containing Co^{2+} and Ni^{2+} ions, followed by the addition of 2-methylimidazole and hexadecyl trimethyl ammonium bromide (CTAB), with continuous stirring at room temperature.

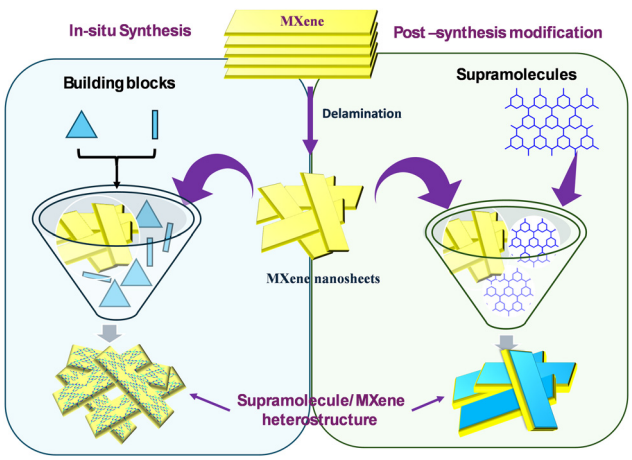

Fig. 6 Synthesis of heterostructures *via in situ* and post-synthesis modification.

The process of COF/MXene hybrid formation is similar to that of MOF/MXene hybrids, with the only difference being the use of metal ions in MOFs whereas only organic molecules are used for the formation of COF/MXene. Geng *et al.*[95] reported *in situ* synthesis of a series of COF@MXene heterostructures through the formation of covalent bonds between the terminal C–O groups of anthraquinone (AQ)-COFs and amino units of modified MXene nanosheets. Similarly Zhao *et al.*[96] and Gong *et al.*[97] reported a solid-phase micro-extraction coating method and an electrostatic self-assembly method for the preparation of COF/MXene heterostructures.

5.2 Post-synthesis modification

This method involves the integration of synthesized supramolecules with MXenes through various approaches, such as mechanical mixing, self-assembly and electrochemical methods, depending on the desired properties of composites and their application. Direct or mechanical mixing and sonication are easy and effective approaches for the preparation of hybrid materials. Non-covalent interactions formed between the components help simultaneously increase the properties of hybrid materials. Wei *et al.*[98] prepared MXene/COF-LZU1 composite films through an ultrasound treatment by the addition of COF particles into the MXene solution. In the direct mixing method, both components, pre-synthesized supramolecules and MXenes, are mixed in a solution to form supramolecule/MXene composites. For example, Wang *et al.*[99] fabricated a novel MIL-100(Fe)/Ti_3C_2 microporous photocatalyst by directly mixing a MOF solution with MXenes for improved nitrogen fixation ability.

In a self-assembly synthesis method, electrostatic interactions, π–π stacking, hydrogen bonding and other interactions are mainly responsible for forming an ordered structure. Liu *et al.*[100] synthesized three dimensional NiCo-MOF/Ti_3C_2 nanosheets through self-assembly. During the self-assembly process, hydrogen bonds were formed between 2D MXene and NiCo-MOF nanosheets. Similarly, Sun *et al.*[101] fabricated a new Co-ZIF-9/MXene photocatalyst through the electrostatic self-assembly method for hydrogen generation.

6. Advantages of hybrid structures over individual components

In photocatalytic reactions, pure supramolecules have many limitations like-low stability, rapid charge carriers' recombination and fast agglomeration after a few cycles, which restrict their photocatalytic application on a large-scale. The compounding of supramolecules with MXenes not only alleviates the aforementioned limitations but also enhances the activity of supramolecules through synergy. In this review, we discuss the newly generated functionalities arising from the combination of MXenes with supramolecules in detail (Fig. 7).

6.1 Improved stability

In some MOFs, poor stability limits their large-scale application, which could be enhanced by rational integration with

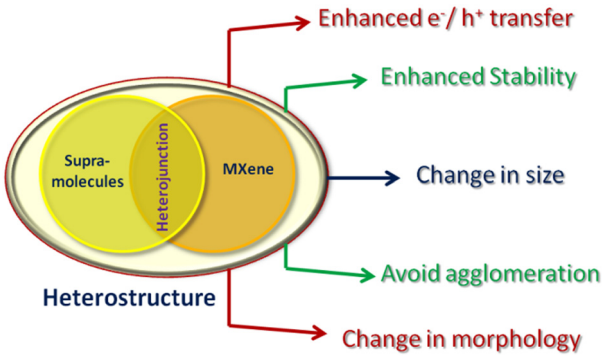

Fig. 7 Advantages of heterostructures, formed by the combination of supramolecules with MXenes.

other materials to produce a synergic effect. Liu *et al.*[100] improved the stability of a bimetallic (Ni–Co) MOF by the formation of hydrogen bonds with Ti_3C_2 MXenes in three-dimensional inter-connected hierarchical porous composites, named Ti_3C_2/NiCo-MOF. Xioan *et al.*[102] prevented the oxidation of MXenes by incorporating lignin into $Ti_3C_2T_x$/NiCo-MOF heterostructures, where the hydroxyl group of lignin formed bonds with the carboxylic group of MOFs and the terminal (T_x) group of MXenes. Wang *et al.*[103] prevented restacking of MXene nanosheets by the formation of electrostatic attraction between two-dimensional Cu-HHTP MOFs and MXenes. Zhao *et al.*[104] improved the cyclic stability of MXenes through electrostatic integration with ZIF derived layered double hydroxide nanosheets, where the surfaces of metal oxides were coated with MXenes to prevent the structural alteration of the electrode. In another study, Wei *et al.*[105] improved the stability by forming a hollow core–shell structure in which binary-metal oxide $ZnCo_2O_4$ formed the core, coated by the Ti_3C_2 layer.

6.2 Change in morphology

The combination of MXenes with MOFs also modifies the morphology of MOFs by creating new interactions with functionality of ligands as well as the bonded central metal center. Ruan *et al.*[106] successfully modulated the rough sheet morphology into a typical dendrite structure by adding MXene suspension (Fig. 8(a)). These structures consisted a thick truck and delicate branches, which were wrapped in MXene nanosheets (Fig. 8(b)–(d)). These unique nano-trees served as electro-active sites where the wrapped conductive MXenes facilitated charge transfer. Zhang *et al.*[107] also modulated the freely grown 2D nanosheet structure (Ni-MOF) into a layered microstrip. The functionality of composite materials was further enhanced by introducing TiO_2 between MXenes and MOFs. Similarly, Wu *et al.*[39] induced morphological changes in the nanosheet structure of the NH_2-MIL-125(Ti) MOF by adding different concentrations of MXenes (Fig. 8(e)–(h)). With 0.1 wt% MXene, nanosheet structures were transformed to rod-shaped nanoparticles (Fig. 7(f)). At higher concentrations [MT1 (1%) and MT5 (5%)], TiO_2 nanosheets and nanoparticles were uniformly dispersed on the surface (Fig. 8(g) and (h)), respectively. This demonstrated the modulating effect of Ti_3C_2 during crystallization.

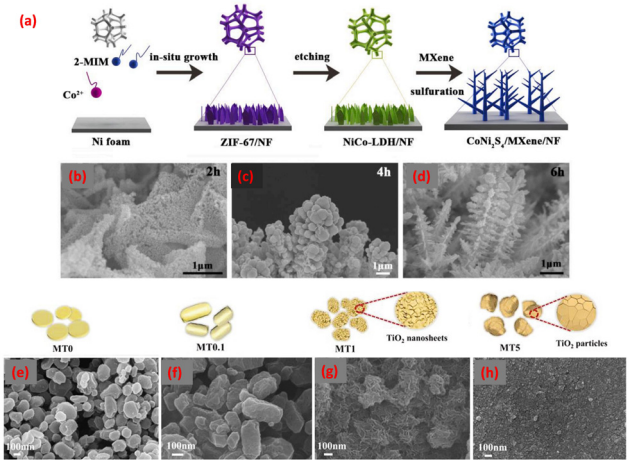

Fig. 8 (a) Synthesis scheme for the $CoNi_2S_4$/MXene/NF hybrid; (b)–(d) SEM images of growth of the $CoNi_2S_4$/MXene/NF hybrid with time (reprinted with permission from ref. 106. Copyright 2021 Elsevier); and (e)–(h) different morphologies of the NH_2-MIL-125(Ti)/MXene hybrid with different contents of MXenes. Reprinted with permission from ref. 39. Copyright 2020 Elsevier.

6.3 Controlled agglomeration

An important advantage in forming composite materials is to decrease the chance of agglomeration. In composite materials of supramolecules with MXenes, the interactions between the free functional group of supramolecules and the group present on the surface of MXenes must be considered. This interaction not only reduces the agglomeration but also simultaneously improves the activity and recyclability of the composite materials. Yang *et al.*[108] controlled the agglomeration of MXenes by uniformly anchoring nanosheets of $CoSe_2$/Ni_3Se_4 on both sides. This anchoring prevented the restacking of MXene sheets and the synergistic effect of MXene@$CoSe_2$/Ni_3Se simultaneously improved the performance, enhanced charge transfer dynamics and increased recyclability.

6.4 Improved electron/ion transport

Supramolecules are advanced materials for photocatalytic activity due to their designed tunable structures, high specific surface areas and porosity. These features not only increase the availability of active sites but also create spaces for the adsorption of catalytic materials. However, the main drawback is the quick recombination of charge carriers. In a supramolecule/MXene heterostructure, the interface formed at the junction facilitates charge transfer between the supramolecules and MXenes, while the low Fermi level of MXenes acts as a driving force for electron transfer from the supramolecules to MXenes[109,110] (Fig. 9). Additionally, the presence of terminal functional groups on MXenes (T_x) and MOFs formed strong interactions during the self-assembly process, which also reduce the transfer pathway of charge carriers. Cheng *et al.*[111] demonstrated that a 2D/2D UNiMOF/Ti_3C_2 hybrid exhibited four times higher photocatalytic activity compared to a bare ultrathin nickel metal organic framework, UniMOF. This is attributed to the smooth transfer of electrons from MOFs to

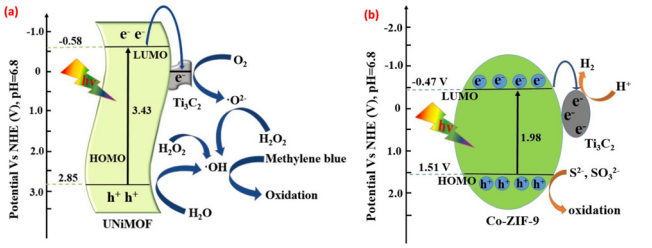

Fig. 9 (a) Band alignment in the UNiMOF/Ti_3C_2 hybrid (reprinted with permission from ref. 111. Copyright 2021 Elsevier) and (b) band alignment in the Co-ZIF-9/Ti_3C_2 heterostructure (reprinted with permission from ref. 101. Copyright 2022 Wiley-VCH GmbH).

the Fermi level of MXenes and the reduced recombination of charge carriers (Fig. 9(a)). Similarly, Sun *et al.*[101] reported high hydrogen production (3538.5 μmol g^{-1} h^{-1}) *via* a photocatalytic reaction over a noble metal free 2D/2D Co-ZIF-9/Ti_3C_2 heterostructure, which was 9.6 times higher than that of Co-ZIF-9 alone due to the efficient transfer and separation of photogenerated electron–hole pairs (Fig. 9(b)).

7. Applications

7.1 Hydrogen generation

In recent years, the depletion of fossil fuels underscored the importance of sustainable fuels with minimal carbon footprints. The demand for clean hydrogen sourced from low-carbon outlets is projected to increase substantially, with estimates indicating a potential annual demand of 200 million metric tonnes by 2030, a substantial rise from the 71 million tonnes recorded in 2019.[112] Among the various technologies (fossil fuel reforming, electrolysis, plasma reforming, and biomass) available for hydrogen production, photocatalytic water splitting stands out as an environmentally friendly approach to replace fossil fuels. In photocatalytic hydrogen generation, water is split into oxygen and hydrogen through the effect of solar light[113] (Fig. 10). The kinetic behaviour of this procedure can be influenced by several factors, such as alterations in pH during the reactions, the concentration of the immediate substrate, and the light absorption capacity of the suspended particles.[114] Tian *et al.*[29] used MXenes as non-metallic co-catalysts in combination with UiO-66-NH_2 MOFs as ideal candidates for photocatalytic hydrogen

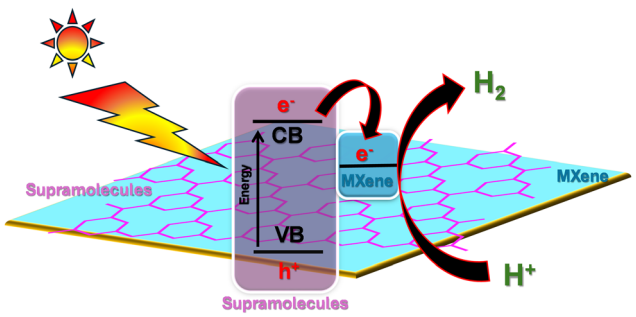

Fig. 10 Pictorial representation of photocatalytic hydrogen production over supramolecule/MXene heterostructures.

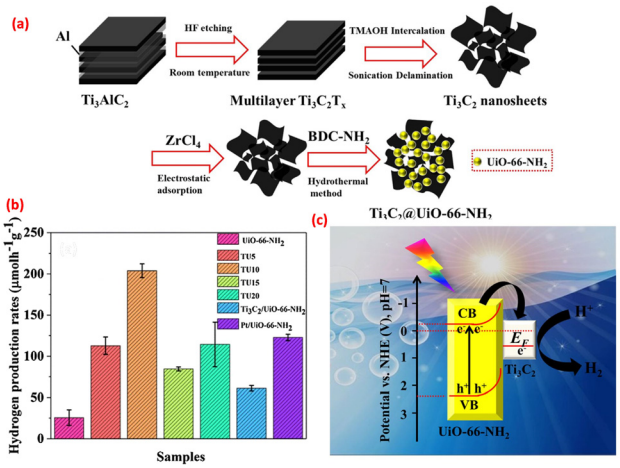

Fig. 11 (a) Synthesis scheme of the TU series; (b) H_2-generation rates under photocatalytic conditions of samples; and (c) proposed mechanism. Reprinted with permission from ref. 29 Copyright 2019 Elsevier.

generation activity. MXene nanosheets, prepared by the intercalation method, were formed in intimate face to face contact with the UiO-66-NH_2 porous MOF prepared by a hydrothermal method (Fig. 11(a)). The synthesized samples were labeled as TU-*X* where *X* represents the dilution concentration of the original MXene concentration by 5, 10, 15 and 20 times. Both the MOF and TU10 exhibited a typical type I hysteresis loop in their nitrogen adsorption and desorption profile, indicating their microporous nature. Further BJH analysis showed that TU10 was more porous than the pristine MOF itself, supporting the fact that MXenes acted as substrates for the growth of UiO-66-NH_2.[115] A comparative photocatalytic study showed that TU10 had the highest photocatalytic hydrogen generation activity, approximately 8-fold greater than that of the bare MOF (Fig. 11(b)). In the TU series, the Schottky junction formed at the interfaces not only suppressed the recombination of electron–hole pairs but also promoted the spatial separation and transfer of charge carriers (Fig. 11(c)). The photocatalytic activity was also further enhanced by the electron-donating ability of MXenes due to the accumulation of photo-induced electrons at the interface. Additionally, DFT calculations supported that O-terminated MXenes showed high photocatalytic activity due to their most positive Fermi level and the lowest Gibbs free energy ($|\Delta G_{H^*}| = 0.08 \approx 0$).[29]

Zhu *et al.*[31] fabricated a nano-hybrid with matched dimensions (2D on 2D) by combining two-dimensional porphyrin-based metal–organic frameworks (Cu-PMOFs) on two-dimensional MXene/TiO_2 nanosheets using a solvothermal reaction at a temperature 120 °C. This ternary photocatalyst demonstrated significantly enhanced photocatalytic hydrogen generation activity, nearly 29-fold that of bare TiO_2. The VB of Cu-PMOFs was more negative than that of TiO_2, facilitating the transfer of holes from TiO_2 to Cu-PMOFs which was very weak and consumed by the TEOA sacrificial reagent. Simultaneously, the electrons present in Cu-PMOFs were transferred at the interface of Cu-PMOFs and TiO_2. In the composite, TiO_2 also acted as a semiconductor and the photogenerated electron also present in the VB of TiO_2. Thus, the VB electron of TiO_2 along

with the electrons present at interfaces flowed to a lower Fermi level of MXenes and reacted with water to produce hydrogen. Thus, the synergistic effect between Cu-PMOFs and Ti_3C_2/TiO_2 enhanced the activity in the visible range, suppressed the recombination of charge carriers and also improved the recyclability. Similarly, Chen *et al.*[32] also fabricated a ternary photocatalyst by compounding Cu-TMOFs with Cu^{2+} anchored to the partially oxidized MXene (TT) as the nucleation sites. The morphology of the TT/Cu-TMOF composite consisted of thin, sheet-like structures with tight interfacial contact. The photocatalytic activity of the nanocomposite (TT/Cu-TMOF) was about 55-fold higher than that of pure TT and also demonstrated high cycle stability.

Due to their layered structure, MXenes can be used as substrates for the growth of supramolecules, which not only facilitates the *in situ* formation of connections but also increases the uniform porosity of supramolecules. Li *et al.*[33] developed a Ti-based MOF (MIL-NH_2) by *in situ* growth onto layered Ti_3C_2 MXenes. Here, MXenes served as both a substrate and a source of Ti for MOF formation. In the composite, the $-NH_2$ group in the MIL-NH_2 MOF coordinated with the Ti atom in Ti_3C_2, accelerating the electron transfer through interfacial contact and simultaneously enhancing the separation efficiency. As a result, Ti_3C_2@MIL-NH_2 (4383 μmol h^{-1} g^{-1}) exhibited higher hydrogen generation performance than bare materials. Similarly, Liu *et al.*[34] synthesized a novel ternary MXene quantum dot based photocatalyst, NH_2-MIL-125(Ti)/MXene quantum dot/$ZnIn_2S_4$ (Ti-MOF/QD/ZIS), to evaluate hydrogen generation activity (2932 μmol g^{-1} h^{-1}) under visible light irradiation. MXene quantum dots acted as a bridge between the semiconducting components for the Z-scheme mechanism and facilitated the transfer of electrons from MOFs to $ZnIn_2S_4$.

Similar to MOFs, the integration of COFs with MXenes not only improves the photocatalytic activity but also significantly enhances the stability of composite materials compared to bare materials. Wang *et al.*[35] synthesized COFs through an acid-catalyzed Schiff base reaction with variation in the ratio of β-ketoenamine to imine as shown in Fig. 12(a). During integration with amine functionalized MXenes, covalent connections were formed between β-ketoenamine-linked COFs and the $-NH_2$ group of MXenes. The increased number of hydroxy groups (–OH) which participated in the formation of β-ketoenamine linkages directly affects the HOMO energy. In photocatalytic activity, an *in situ* synthesized COF/MXene hybrid (ATNT) showed a higher hydrogen generation yield in comparison to physical mixing samples. The enhancement in activity was due to the formation of heterojunctions in ATNT hybrids which provided short pathways for the transfer of photogenerated electrons through the synergistic effect of photoactive COFs and amine functionalized conductive MXenes. Most importantly, the hybrid with optimized content of MXene (ATNT-4) showed higher photocatalytic activity as an increase in content of amine functionalized MXenes blocked the active site and also shielded open areas for light absorption (Fig. 12(b)). Recyclability experiments demonstrated that the COF hybrid had high recyclability (more than 6 cycles) (Fig. 12(c)) and good stability.

In addition to the above binary examples (supramolecule/MXene), Tian *et al.*[30] used annealed MXenes ($Ti_3C_2T_x$) for the synthesis of a ternary photocatalyst for hydrogen production. During the annealing process, MXenes retained their original layered structure with the formation of TiO_2, which combined with a water-stable porous UiO-66-NH_2 MOF to form a layered porous ternary catalyst (Ti_3C_2/TiO_2/UiO-66-NH_2). Detailed structural analysis with FE-SEM and TEM showed that all the three components of the ternary catalyst (MOF, titanium dioxide and Ti_3C_2) were arranged in such a manner that they formed three types of contact interfaces: MXene/TiO_2/MOF, MXene/TiO_2, and MXene/MOF. The N_2 adsorption–desorption isotherms showed that the ternary catalyst (988 m^2 g^{-1}) had a slightly higher specific surface area with a microporous structure compared to the pure MOF (977 m^2 g^{-1}). In a porous ternary catalyst, three interfaces were formed at the contact of the MOF, TiO_2 and MXene. These three interfaces initiated three pathways for photocatalytic hydrogen generation (1980 mmol h^{-1} g^{-1}) in the ternary catalyst which was higher than that of pristine UiO-66-NH_2 under simulated sunlight irradiation. In pathway-I, the photogenerated electron was directly transferred to the Fermi level of TiO_2 from the MOF, suppressing the recombination of charge carriers. In pathway-II, the photocatalytic generated electron present in the conduction band of TiO_2 is directly transferred to Ti_3C_2 for further photocatalytic activity. In pathway-III, the photogenerated electron in the conduction band of the MOF was directly transferred to TiO_2 which was then indirectly transferred to Ti_3C_2 for further activity. Thus, the synergistic effect of all three components, formed through three contact interfaces, was mainly responsible for the enhanced photocatalytic activity and for successfully suppressing the recombination of charge carriers. This was also confirmed by the low PL intensity of the ternary composite in comparison to other bare components. This work established a foundation for MOF-based ternary photocatalysts for further studies in the field of photocatalytic hydrogen generation activity.

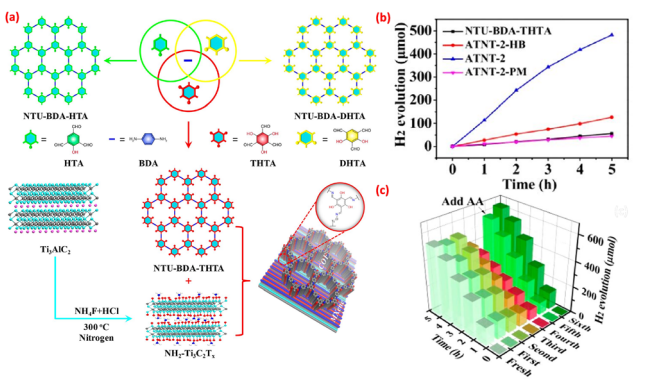

Fig. 12 (a) Synthesis of the COF/MXene–NH_2 hybrid; (b) photocatalytic activity of synthesized hybrids; and (c) recyclability. Reprinted with permission from ref. 35. Copyright 2020 American Chemical Society.

7.2 Pollutant degradation

Statistical estimations indicate that industries using organic dyes for manufacturing and applications in textile, pharmaceuticals,

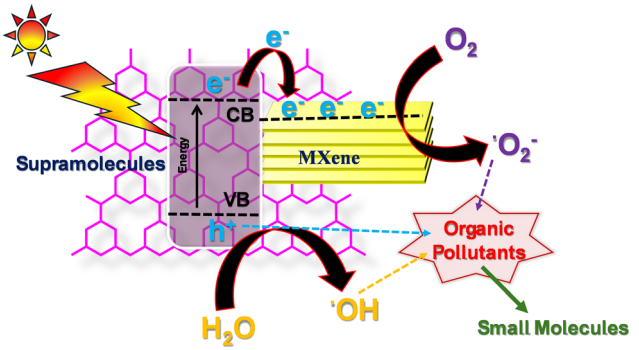

Fig. 13 Pictorial representation of photocatalytic degradation of organic pollutants over supramolecule/MXene heterostructures.

leather, pulp and paper, personal care products and food processing produce over 700 000 tons of organic dyes globally each year. Approximately, 10–15% of these dyes are released as waste effluents.[116] In comparison to other methods such as ozonation,[117,118] adsorption[119,120] and filtration[121,122] degradation of pollutants through the photocatalytic method is one of the preferred approaches. This method is simple, energy-efficient, low-cost and stable, with a minimal production of secondary pollutants. In photocatalytic degradation, semiconductor materials absorb light with enough energy to transfer electrons from the valence band (VB) to conduction band (CB), leading to the generation of oxidative holes in the valence band (VB). Highly reactive species are produced from the reaction of reductive electron and oxidative holes with dissolved oxygen/H_2O/H_2O_2 which can directly degrade the large molecular structure of pollutants to small molecules (monomers, CO_2 *etc.*) (Fig. 13). Additionally, the role of active species in the degradation process can also be investigated by scavenger tests. In these tests, scavengers, such as potassium iodide (KI), *p*-benzoquinone (*p*-BQ), and isopropyl alcohol (IPA), are added to the reaction mixture to capture the holes (h^+), superoxide ions ($^\bullet O^{2-}$) and hydroxyl radical ($^\bullet$OH), respectively. A detailed review of the photocatalytic activity of supramolecular/MXene composites for pollutant degradation is summarized in Table 1.

In supramolecules, the fast recombination of photocatalytically generated charge carriers can be controlled by the compounding of supramolecules with MXenes which can abstract the electron to the low Fermi level. This synergistic effect of composite materials can significantly enhance the efficiency of pollutant degradation. Far *et al.*[36] developed a highly efficient MXOF photocatalyst by decorating $Ti_3C_2T_x$ MXene nanosheets with a highly porous ZIF-8 MOF under solvothermal conditions. In the MXOF photocatalyst, spherical ZIF-8 nanoparticles (<100 nm) were uniformly distributed on the MXene nanosheets. The MXOF, with a specific surface area of 37.7 $m^2\ g^{-1}$, was mesoporous in nature whereas the bare MOF was microporous with a specific surface area of 851 $m^2\ g^{-1}$. In this heterostructure, the MXOF benefited from a tunable band gap of 4.99 eV which was intermediate between the bare MXene (5.18 eV) and MOF (4.79 eV). This tunable band gap not only enhanced the charge transfer but also reduced the recombination rate of photogenerated charge carriers through the transfer of electrons between the band of MOFs and MXene. The synergistic effect of both components resulted in impressive photodegradation efficiency, achieving 62% degradation of methylene blue (MB) and 35% degradation of Direct Red 31 (DR31) dyes, along with excellent recyclability. Additionally, scavenger tests were also performed which showed that the photodegradation efficiency of the DR31 dye with and without *p*-BQ was 35%, whereas photodegradation of MB was 62% and 48% with and without *p*-BQ respectively. These results indicated that $^\bullet O^{2-}$ did not play a major role in the photodegradation of DR31.

Similarly, Cao *et al.*[37] also reported a MOF–MXene photocatalyst that showed 96% degradation of the tetracycline (TC) pollutant after 90 min of photocatalysis, with a mineralization rate of 45.5%. In the solvothermally synthesized bimetallic/MXene (Sn–Bi–MOF/Ti_3C_2) heterostructure, bulk MXene (Ti_3C_2) had a multilayered structure with a layer spacing ranging from 75 to 240 nm while bimetallic Sn–Bi–MOF nanoparticles had small particles (nearly 60 nm size) with rough surface and slight agglomeration. The degree of agglomeration of the bimetallic MOF was effectively low in MXOF composites. MXenes, bimetallic Sn–Bi–MOF, and MXOF catalysts were all mesoporous and have type IV isotherms with H_3-type hysteresis loops. However, the MXOF had a higher specific surface area, pore volume, and pore diameter than the bare MXene and bimetallic MOF, providing more active sites for the photocatalytic degradation reaction. The photocatalytic mechanism of Sn–Bi–MOF/Ti_3C_2 showed that the Schottky junction formed at the surface of MOFs and MXenes accelerated the transfer of photogenerated electrons to MXenes and enhanced charge separation and led to free radical generation. In the degradation process, $^\bullet O_2$ and h^+ are the main active substances. The recyclability of the Sn–Bi–MOF/Ti_3C_2 composite was good even after four cycles of the photocatalytic experiment, which was further confirmed by PXRD patterns of samples before and after the reaction.

In photocatalysis, the enhanced activity of composite materials compared to bare materials is mainly due to the formation of a heterojunction at the surface, which promotes the transfer of charge carriers through heterojunction barriers and decreases the rate of recombination. However, in some cases, the controlled morphology of materials acts as a supporting factor to enhance the activity, as reported by Tan *et al.*[38] The morphology of the photocatalyst was controlled by the H_2O–DMF solvent ratio during the synthesis process. Different morphologies of the MIL-88A(Fe) MOF, from elongated spindle shape to short spindle shape, were obtained by decreasing the H_2O ratio in the H_2O/DMF mixture, named S-MIL-88A(Fe) (in pure water), W-MIL-88A(Fe) (H_2O : DMF 1 : 1) and D-MIL-88A(Fe) (pure DMF) (Fig. 14(a)). These highly stable MIL-88A(Fe) MOFs with modulated active crystal planes were used to form composites with MXenes, creating a type-I heterojunction. This series of composites was named XA-MY where X denotes the morphology such as SA-M100, WA-M100, and DA-M100 and Y denotes the different MXene loadings (DA-M50, DA-M100, and DA-M150). Due to a large elongated structure, S-MIL-88A(Fe) was highly agglomerated on the surface of MXenes in comparison to W-MIL-88A(Fe) and D-MIL-88A(Fe). The DA-M100 composite exhibited the most effective activity, achieving

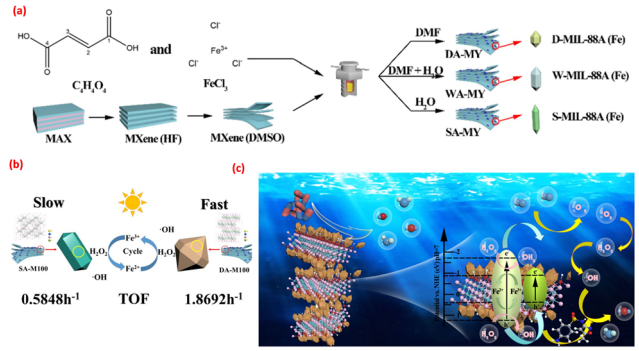

Fig. 14 (a) Synthesis scheme of XA-MY; (b) TOF diagram; and (c) proposed mechanism. Reprinted with permission from ref. 38; Copyright 2024 Elsevier.

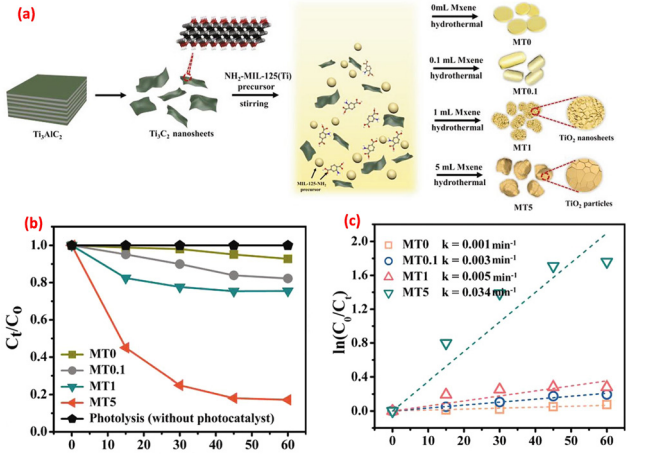

Fig. 15 (a) Synthesis scheme of Ti_3C_2/MOF heterostructures; (b) photocatalytic degradation of TC-HCl ($\lambda > 420$ nm) of all as-synthesized samples; and (c) pseudo first-order kinetic fitting curves. Reprinted with permission from ref. 39. Copyright 2020 Elsevier.

approximately 70% degradation of sulfamethoxazole within 10 minutes of light exposure and reaching 93% efficiency after 60 minutes compared to other samples (Fig. 14(b) and (c)). The rate constant for the degradation of sulfamethoxazole of DA-M100 was 1.03 and 2.37 time higher than that of WA-M100 and SA-M100, respectively. The excess amount of MXenes also masked the active sites of MOFs, resulting in reduction in the catalytic performance of the photocatalyst. Additionally, universality tests demonstrated that DA-M100 acted as a dual photo catalyst, showing strong oxidation efficiency for common dyes and efficient reduction for heavy metal ions in sewage. The removal capabilities for Cr(VI), Cu(II), and Ni(II) were 95.88%, 79.77%, and 66.67%, respectively, after 1 hour of irradiation, indicating good environmental adaptability. A detailed study showed that at the interface, the composite exhibited a type-I heterojunction which was mainly responsible for the transport and separation of photogenerated charge carriers and enhanced photocatalytic activity. Additionally, this work presented a new approach for designing and synthesizing heterostructures with dual reduction and oxidation capabilities.

Similarly, Wu *et al.*[39] also used Ti_3C_2–MXenes as modulators to affect the growth of the MIL-125-NH_2 MOF during the synthesis of nanohybrid structures. As shown in Fig. 15(a), the morphology of the composite changed with the amount of MXene from 0 to 5 mL. MT0 (0 mL MXene with MIL-125-NH_2 MOF) exhibited plate-type nanosheets morphology which changed to rod type morphology (MT0.1) with the addition of 0.1 mL MXene. As the amount of MXene increased, the rod-type structure was converted to enlarged particle morphology with a uniform distribution of TiO_2 nanosheets and nanoparticles on the surface of NH_2-MIL-125(Ti) in MT1 and MT5 respectively, along with a partial loss of the organic ligand (Fig. 15(a)). Due to the presence of the –NH_2 group in the ligand, MT0 showed the characteristics adsorption band at 480 nm,[123] which was further extended to 570 nm with enhanced absorption intensity in MT5 due to a high amount of black-colored MXene. This enhancement in absorption intensity was mainly responsible for the generation of charge carriers and high photocatalytic activity. The optimized photocatalytic degradation efficiency of MT5 nanohybrids towards higher tetracycline hydrochloride (TC-HCl) was 82.80% in 60 min which was 11.5 times higher that of pristine MT0 (MIL-125-NH_2) under visible light irradiation ($\lambda > 420$ nm) (Fig. 15(b)). The order of rate constant is – MT5 (0.034 min^{-1}) > MT1 (0.005 min^{-1}) > MT0.1 (0.003 min^{-1}) > MT0 (0.001 min^{-1}) (Fig. 15(c)). This highest photocatalysis activity of MT5 was mainly due to the presence of a dual heterojunction which not only increased the charge carrier density but also remarkably enhanced the interfacial charge separation as well as transfer. Additionally, the recyclability of MT5 in photocatalytic TC-HCl degradation was approximately 81.00% after four consecutive recycles. This work provided insight into the modification of semiconductor morphology in the presence of a modulator and demonstrated the importance of dual heterojunctions in the hybrid material.

7.3 CO_2 reduction

Carbon dioxide (CO_2) is a greenhouse gas which contributes to nearly 76% of global warming. Thus, the conversion of CO_2 to value-added products by photocatalysis could effectively address the critical issues of climate changes and energy shortages. Research on efficient photocatalysts for CO_2 reduction is still in its early stage. The regeneration of photocatalytic nicotinamide adenine dinucleotide (NADH) conjugated with enzymatic CO_2 reduction is crucial for global sustainable development. Wei *et al.*[40] synthesized a rationally designed lawn-like TP-COF/$Ti_3C_2T_x$ (TCM) photocatalyst by the *in situ* and post synthesized loading of COFs on NH_2 functionalized $Ti_3C_2T_x$-MXenes for NADH regeneration. The synthesized hybrid samples were labeled as TCM-*y*%, where *y*% denotes the MXene percentage ranging from 5% to 20% resulting in TCM-5%, TCM-10%, TCM-15%, and TCM-20%, respectively. As shown in Fig. 16(a), in the presence of an electron mediator, the order of photocatalysts for the formate yield was TCM-15% (11.9 mmol L^{-1}) > TCM-10% (8.0 mmol L^{-1}) > TCM-20% (6.3 mmol L^{-1}) > TCM-5% (5.9 mmol L^{-1}) > TC (5.4 mmol L^{-1}), demonstrating the crucial role of NADH in the FDH-catalyzed CO_2 reduction reaction. Similarly, in the absence of an electron mediator, the order of photocatalysts for the formate

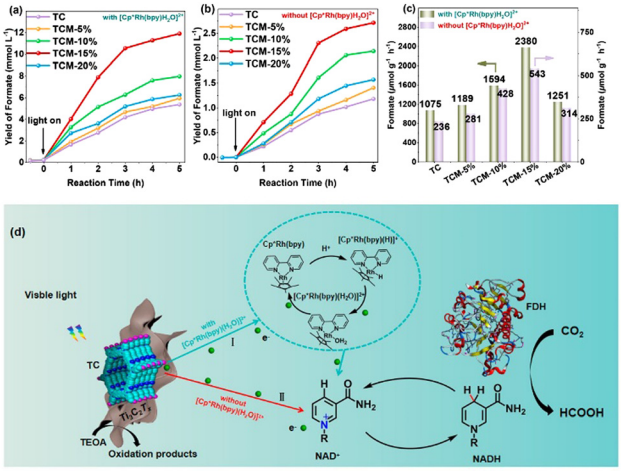

Fig. 16 Formate yields (a) with and (b) without an electron mediator. (c) Comparison of production rates and (d) possible mechanism. Reprinted with permission from ref. 40. Copyright 2024 American Chemical Society.

yield was TCM-15% (2.7 mmol L^{-1}) > TCM-10% (2.1 mmol L^{-1}) > TCM-20% (1.6 mmol L^{-1}) > TCM-5% (1.4 mmol L^{-1}) > TC (1.2 mmol L^{-1}) as shown in Fig. 16(b). Thus, the NADH regeneration yield achieved by TCM-15% was nearly 95% and 46% with and without an electron mediator ($[Cp^*Rh\text{-}(bpy)(H_2O)]^{2+}$) respectively, whereas TP-COFs achieved only 42% with an electron mediator (Fig. 16(c) and (d)). Also, the TOF value for NADH regeneration was about 4.05 and 4.90 times higher than those of pure TP-COFs, with and without an electron mediator, respectively. This work established a strong foundation for efficiently achieving NADH regeneration without the need for an electron mediator.

Li *et al.*[41] *in situ* grew a ZIF-66 MOF (zeolitic imidazolate framework-67) on the surface of MXenes using a self-assembly method. The addition of Co salts followed by 2-MIM in MXene solution allowed the MOFs to grow on the MXene surface. The ZIF-67/$Ti_3C_2T_x$ MXene photocatalyst is denoted as ZT-*a*, where *a* (= 90, 180, 270, 360, 450, 540, and 630 mg) represents the specific weight of MXenes. The polyhedral structure of ZIF-67 was distributed on the layered surface of MXenes. The Schottky heterojunction formed at the junction of ZIF-67 and MXenes in ZT-450 showed the smooth transfer of electrons from ZIF-67 to $Ti_3C_2T_x$, indicating the highest rate of separation and longest lifetime of photogenerated charge carriers. Among the other synthesized composites, ZT-450 showed the highest activity towards photocatalytic CO_2 reduction yielding carbon monoxide (CO), methane (CH_4), and hydrogen (H_2) at 62.7, 6.7, and 7.3 μmol g^{-1}, respectively. The production of CO over ZT-450 was 16 and 4.8 higher than that of bare ZIF-67 and $Ti_3C_2T_x$, respectively, due to higher adsorption ability of CO_2 in ZT-450 (127.90 μmol g^{-1}). *In situ* DRIFTS measurements revealed the presence of intermediates such as *COOH, *CHO, *OCH_3, *etc.* during the photocatalytic CO reduction reaction (CO_2RR) on the photocatalyst. In the heterostructure, the excited electrons of ZIF-67 were transferred to the Fermi level of $Ti_3C_2T_x$ facilitating the CO_2 reduction reaction. Meanwhile, the holes in the valence band of ZIF-67 drove the oxidation reactions to generate O_2. This localized separation of charge carriers in heterostructures was mainly responsible for the enhancement of photocatalytic efficiency.

According to theoretical calculations, the photocatalytic activity of MXenes can be improved through the formation of a Schottky junction by coupling with a n-type semiconductor that has a smaller work function than that of MXenes. Song *et al.*[42] synthesized a ternary heterostructure with a Z-scheme heterojunction by combining two semiconductors with highly conductive MXenes. In a ternary photocatalyst, porous flakes of g-carbon nitride were loaded with the clusters of the Sn–Bi–MOF that wrapped around the layered structure of MXenes. Under simulated sunlight, the reduction of CO_2 to CO over the ternary g-CN/TC/SBM composite was 36.33 μmol g^{-1} h^{-1}, which was 4.36-fold that of g-carbon nitride and 3.5-fold that of SBM. The quantum apparent efficiency (AQY) was 3.2% at 420 nm. In ternary composites, three interfaces formed at the junctions of surfaces which were responsible for the transfer of charge carriers in the Z-scheme. In the presence of light, the photogenerated electrons moved to the low Fermi level of MXenes and formed a barrier at the surface, controlling the reflow of electrons from MXenes to g-carbon nitride. Simultaneously, these electrons accelerated to the Sn–Bi–MOF due to the Schottky barrier formed with MXenes. Thus, this Z-scheme Schottky barrier not only separated the charge carrier but also controlled the recombination of electrons and holes which was mainly responsible for the increased production of CO. Chen *et al.*[43] also demonstrated the significance of three dimensional hybrid structures, Co–Co LDH/TNS composites, based on MXenes as a promising candidate for photoreduction of CO_2 to value added products. In a 3D hierarchical nanoarray, Co acted as active species and was mainly responsible for the significant enhancement of the CO_2-to-CO conversion rate (1.25×10^4 μmol h^{-1} g^{-1}) and excellent stability (Fig. 17).

7.4 Antibacterial activity

In marine engineering, marine fouling is an emerging problem that negatively impacts the environment and human health. Thus, it is crucial for researchers to develop efficient, highly

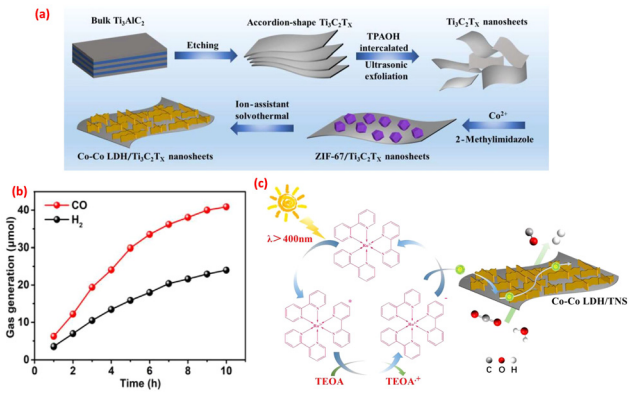

Fig. 17 (a) Synthesis scheme of Co–Co LDH/TNS nanosheets; (b) release of CO and H_2 with time intervals; and (c) proposed mechanism. Reprinted with permission from ref. 43. Copyright 2020 Elsevier.

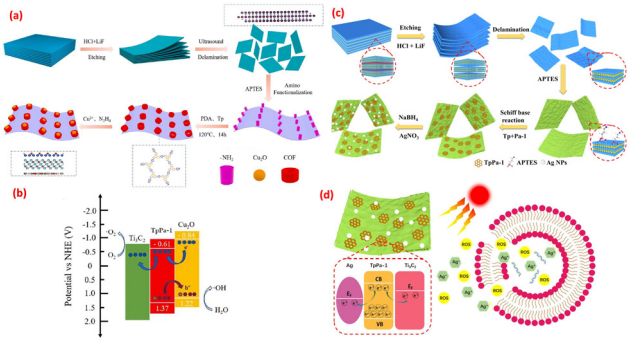

Fig. 18 (a) Synthesis scheme of Ti_3C_2/TpPa-1/Cu_2O; (b) proposed mechanism, reprinted with permission from ref. 45. Copyright 2022 Elsevier; (c) synthesis scheme of Ti_3C_2/TpPa-1/Ag; and (d) proposed antibacterial mechanism. Reprinted with permission from ref. 46. Copyright 2023 Elsevier.

active and environment friendly antifouling agents that can function under normal environmental conditions. One emerging concept is the use of an antifouling agent that can be activated under sunlight. However, traditional semiconductors such as TiO_2,[124] ZnO,[125] CuO,[126] MoS_2[127] *etc.* suffer from the major disadvantage of fast recombination of charge carriers. Thus, Liu *et al.*[44] *in situ* grew a TpPa-COF semiconductor on the surface of highly conductive MXenes through the Schiff base reaction, which simultaneously anchored the metal oxide nanoparticles (Cu_2O NPs) through covalent bonding to obtain a highly efficient photocatalytic bactericide (Fig. 18(a)). In the ternary photocatalyst, Ti_3C_2/TpPa-1/Cu_2O and TpPa-COF acted as semiconductors. Heterojunctions formed between TpPa-1 and Cu_2O facilitated the migration of photogenerated charge carriers. Due to their excellent conductivity and surface plasmon resonance effect, MXenes promoted the transport of charge carriers and acted as co-catalysts (Fig. 18(b)). The high porosity of TpPa-1 with large pore size/volume reduced the lattice density and enhanced the contact of active site with medium, along with improving the storage of active oxygen species. This synergistic effect of all three components in the ternary photocatalyst was mainly responsible for high antibacterial properties against *P. aeruginosa* and *S. aureus*, with antibacterial rates of 99.62% and 98.90% which were 33% and 50% higher in comparison to the bare TpPa-1-COF. This combination of the ternary catalyst not only improved the active transport of charge carriers but also reduced the chance of photocorrosion.

Similar to Cu_2O which released the Cu^{2+} during the sterilization process, Ag nanoparticles also have importance in sterilization as they release Ag^+ which enhance the activity in the visible region but also have large work function to accelerate the migration of electrons. Wang *et al.*[45] utilized this advantage and developed a Ag NP-based ternary photocatalyst to achieve a highly active photocatalytic antifouling material. Similar to the method mentioned above, Ti_3C_2/TpPa-1/Ag was obtained by *in situ* growth of a COF on the 2D surface of MXenes through the Schiff base reaction, followed by covalent anchoring of Ag nanoparticles (Fig. 18(c)). The surface plasmon resonance (SPR) phenomenon of both MXenes and Ag NPs was mainly responsible for the transfer of electrons from the TpPa-COF to the Fermi level of MXenes and Ag NPs through a Schottky barrier (Fig. 18(d)). Additionally, the ternary composite controlled the release of Ag^+ ions, enhancing antibacterial efficacy. The higher electron transport and lower electron–hole recombination activities of the Ti_3C_2/TpPa-1/Ag ternary system contributed to its efficiency. Due to the synergistic effect of all the three components, the ternary composite (Ti_3C_2/TpPa-1/Ag) demonstrated a superior antibacterial activity against *S. aureus* and *P. aeruginosa*, with antibacterial rates reaching 99.60% and 99.78%, respectively.

MOFs consisting of suitable bioactive metal ions and functionalized organic ligands also showed excellent antibacterial activity. Li *et al.*[46] grew the porphyrin based porous 2D MOF (Cu-TCPP) nanosheets *in situ* on the layered Ti_3C_2–MXene to form a Cu-TCPP/Ti_3C_2 composite for bacteria-killing efficiency under photocatalytic conditions. The conjugation of MOFs with MXenes formed a Schottky barrier and a space charge layer at the interface due to the difference in work functions. Under light irradiation, photocatalytically generated electrons were transferred to the MXenes through Schottky barriers, enhancing the separation of charge carriers by inhibiting the backflow of electrons from MXenes. As a result, more ROS were produced and over 99% of *S. aureus* were killed over the MOF/Ti_3C_2 composite. This work provided deeper insights into designing MOF-based composites with high photophysical properties through *in situ* interfacial engineering strategies for photocatalytic antibacterial activity.

8. Challenges and future perspectives

Regardless of promising and remarkable improvement of supramolecules/MXene heterostructures in few years, several challenges still need to be overcome to fully explore their potential and make sure their transition from low scale laboratory research to large scale real-world applications. This section will focus on these challenges, their potential solutions and future perspectives in this rapidly growing research field.

Despite the many reported works on the synthesis of hybrid materials, the synthesis of supramolecules/MXenes is not an easy task. MXenes have the tendency to form staking layered structures which are connected through weak bonding. Sometime, this behavior restricts the synthesis of heterostructures with supramolecules. Thus, a controlled synthesis process is required for the uniform distribution and interface formation between supramolecules and MXenes. Low stability of supramolecules is still a challenge which can be controlled by uniform layering of supramolecules over MXenes. This layering can be controlled by the interaction formed between supramolecules and MXenes. Otherwise, supramolecular frameworks may collapse and consequently decrease the performance and recyclability. Thus, rational design of heterostructures and their accurate characterization are still crucial challenges because of the complex design of heterostructures and overlapping of properties of all components. These challenges can

be solved by the development of advanced characterization techniques that can give comprehensive data about the structure, involved interactions, morphology and properties.

The ultimate objective of the research is the commercialization of prepared materials in desired applications, which is another significant challenge. This commercialization is only possible if the material can be produced cost-effectively under safety guidelines and its stability under the given environmental conditions can be ensured. Secondly, because of environmental concerns, the method should be green, that is, without producing hazardous by-products. In the view of next-generation materials, supramolecule/MXene heterostructures have high potential to be used in multiple applications from environmental application to green fuel generation. For the scale-up, more work needs to be done in the field of advance methods and instruments. Furthermore, integration of advanced computational studies, machine learning and artificial intelligence tools with research will help to predict the details of controlled reaction conditions for the synthesis of desired structures and the behavior of designed materials towards novel applications. Thus, the combined efforts of chemical, material and environmental scientists and also engineers will help in the commercialization of supramolecule/MXene heterostructures.

9. Conclusions

In this comprehensive review, a supramolecule/MXene heterostructure is highlighted as a potential candidate for advancing the photocatalytic activity, with applications ranging from green fuel production (hydrogen generation) to addressing environmental problems (such as CO_2 conversion, pollutant degradation, and more). By exploring the unique properties of supramolecules, photocatalytically active tunable porous structures, in combination with highly stable conductive structures of MXenes, these heterostructures can exhibit an enhanced photocatalytic activity simultaneously addressing the inherit stability limitations of supramolecules. The morphology of these heterostructures significantly impacts charge carrier dynamics, stability and recyclability which can be precisely controlled by the modification of synthesis methods, including *in situ* and post-synthesis adjustments. Future research should focus on the development of new synthesis techniques that facilitate new bonding between composite materials and explore their performance in other applications. Overall, the integration of supramolecules with MXenes opens up new opportunities for the development of sustainable materials for photocatalytic applications, contributing to the solution of energy and environmental problems through green technology.

Author contributions

P. Verma: writing – original draft, J. V. Marseveen: writing – review & editing, N. R. Shiju: funding acquisition, supervision, writing – review & editing.

Data availability

No primary research results, software or code have been included, and no new data were generated or analysed as part of this review.

Conflicts of interest

There are no conflicts to declare.

Acknowledgements

P. Verma gratefully acknowledges Research Priority Area (RPA) Sustainable Chemistry of the University of Amsterdam for a postdoctoral fellowship.

Notes and references

1 A. Kudo and Y. Miseki, *Chem. Soc. Rev.*, 2009, **38**(1), 253.
2 K. Wenderich and G. Mul, *Chem. Rev.*, 2016, **116**(23), 14587.
3 A. Fujishima and K. Honda, *Nature*, 1972, **238**(5358), 37.
4 S. A. Rawool, M. R. Pai, A. M. Banerjee, A. Arya, R. S. Ningthoujam, R. Tewari, R. Rao, B. Chalke, P. Ayyub, A. K. Tripathi and S. R. Bharadwaj, *Appl. Catal., B*, 2018, **221**, 443.
5 T. Hisatomi, J. Kubota and K. Domen, *Chem. Soc. Rev.*, 2014, **43**(22), 7520.
6 S. Zhong, Y. Xi, S. Wu, Q. Liu, L. Zhao and S. Bai, *J. Mater. Chem. A*, 2020, **8**(30), 14863.
7 D. Vaya and P. K. Surolia, *Environ. Technol. Innovation*, 2020, **20**, 101128.
8 L. Wang, C. Bie and J. Yu, *Trends Chem.*, 2022, **4**(11), 973.
9 S. Liu, N. Zhang and Y. J. Xu, *Part. Part. Syst. Charact.*, 2014, **31**(5), 540.
10 B. M. McVey and P. J. Cragg, Supramolecules, *Supramolecular Chemistry in Corrosion and Biofouling Protection*, CRC Press, 2021, pp. 3–16.
11 T. R. Cook, Y. R. Zheng and P. J. Stang, *Chem. Rev.*, 2013, **113**(1), 734.
12 X. Wu, Z. Liu, H. Guo, Y. L. Hong, B. Xu, K. Zhang, Y. Nishiyama, W. Jiang, S. Horike, S. Kitagawa and G. Zhang, *ACS Appl. Mater. Interfaces*, 2021, **13**(31), 37172.
13 P. Verma, U. P. Singh and R. J. Butcher, *CrystEngComm*, 2019, **21**(36), 5470.
14 J. Yang, Z. Chen, L. Zhang and Q. Zhang, *ACS Nano*, 2024, **18**(33), 21804.
15 P. Verma, U. P. Singh, T. Verma, R. J. Butcher and P. Mohanty, *J. Coord. Chem.*, 2024, **77**(12), 1566.
16 G. Yuan, L. Tan, P. Wang, Y. Wang, C. Wang, H. Yan and Y. Y. Wang, *Cryst. Growth Des.*, 2021, **22**(1), 893.
17 P. Verma, R. V. Singh, A. M. Banerjee and M. R. Pai, *Int. J. Hydrogen Energy*, 2025, **107**, 569.
18 W. Liang, M. Liu, X. Shi, B. Chen, L. Shao, J. Xu and Z. Sun, *Batteries Supercaps*, 2024, **7**(2), e202300462.
19 X. Shi, W. Liang, G. Liu, B. Chen, L. Shao, Y. Wu, Z. Sun and F. García, *Chem. Eng. J.*, 2023, **462**, 142271.
20 L. Shi, C. Wu, Y. Wang, Y. Dou, D. Yuan, H. Li, H. Huang, Y. Zhang, L. D. Gates, X. Sun and T. Ma, *Adv. Funct. Mater.*, 2022, **32**(30), 2202571.
21 M. Naguib, M. W. Barsoum and Y. Gogotsi, *Adv. Mater.*, 2021, **33**(39), 2103393.
22 T. K. Slot, V. Natu, E. V. Ramos-Fernandez, A. Sepulveda-Escribano, M. Barsoum, G. Rothenberg and N. R. Shiju, *2D Mater.*, 2021, **8**(3), 035003.
23 X. Ma, J. Kang, Y. Wu, C. Pang, S. Li, J. Li, Y. Xiong, J. Luo, M. Wang and Z. Xu, *Chem. Eng. J.*, 2023, **469**, 143888.
24 T. Ramachandran, F. Hamed, Y. A. Kumar, R. K. Raji and H. H. Hegazy, *J. Energy Storage*, 2023, **73**, 109299.
25 A. E. Mathew, S. Jose, A. M. Babu and A. Varghese, *Mater. Today Chem.*, 2024, **36**, 101927.

26 T. K. Slot, F. Yue, H. Xu, E. V. Ramos-Fernandez, A. Sepúlveda-Escribano, Z. Sofer, G. Rothenberg and N. R. Shiju, *2D Mater.*, 2020, **8**(1), 015001.
27 M. Ronda-Lloret, V. S. Marakatti, W. G. Sloof, J. J. Delgado, A. Sepúlveda-Escribano, E. V. Ramos-Fernandez, G. Rothenberg and N. R. Shiju, *ChemSusChem*, 2020, **13**, 6401.
28 W. Ng, E. S. Gnanakumar, E. Batyrev, H. F. Greer, W. Zhou, R. Sakidja, G. Rothenberg, M. Barsoum and N. R. Shiju, *Angew. Chem., Int. Ed.*, 2018, **57**, 1485.
29 P. Tian, X. He, L. Zhao, W. Li, W. Fang, H. Chen, F. Zhang, Z. Huang and H. Wang, *Sol. Energy*, 2019, **188**, 750.
30 P. Tian, X. He, L. Zhao, W. Li, W. Fang, H. Chen, F. zhang, Z. Huang and H. Wang, *Int. J. Hydrogen Energy*, 2019, **44**(2), 788.
31 H. Zhu, Y. Chen, T. Zhang, L. Qin, S. Z. Kang and X. Li, *J. Solid State Chem.*, 2023, **327**, 124298.
32 Y. Chen, H. Zhu, S. Z. Kang, T. Zhang, L. Qin and X. Li, *J. Alloys Compd.*, 2023, **961**, 170929.
33 Y. Li, Y. Liu, Z. Wang, P. Wang, Z. Zheng, H. Cheng, Y. Dai and B. Huang, *Chem. Eng. J.*, 2021, **411**, 128446.
34 S. Liu, X. Jiang, G. I. Waterhouse, Z. M. Zhang and L. M. Yu, *Sep. Purif. Technol.*, 2022, **294**, 121094.
35 H. Wang, C. Qian, J. Liu, Y. Zeng, D. Wang, W. Zhou, L. Gu, H. Wu, G. Liu and Y. Zhao, *J. Am. Chem. Soc.*, 2020, **142**(10), 4862.
36 H. S. Far, M. Najafi, M. Hasanzadeh and R. Rahimi, *Inorg. Chem. Commun.*, 2023, **152**, 110680.
37 Y. Cao, L. Yue, Z. Li, Y. Han, J. Lian, H. Qin and S. He, *Appl. Surf. Sci.*, 2023, **609**, 155191.
38 Q. Tan, Z. Yu, Q. Xiang, N. He, R. Long and J. Wang, *Process Saf. Environ. Prot.*, 2023, **179**, 405–420.
39 Y. Wu, X. Li, Q. Yang, D. Wang, F. Yao, J. Cao, Z. Chen, X. Huang and X. Li, *Chem. Eng. J.*, 2020, **390**, 124519.
40 P. Wei, J. Dong, X. Gao, L. Chang, Z. Huang, H. Zheng, S. M.-Y. Lee, W.-Y. Lou and C. Peng, *ACS Sustainable Chem. Eng.*, 2024, **12**(18), 6881.
41 Z. Li, J. Xiong, H. Song, S. Liu, Y. Huang, Y. Huang, G. I. N. Waterhouse, Z. Wang, Y. Mao, Z. Liang and X. Luo, *Sep. Purif. Technol.*, 2024, **341**, 126817.
42 Z. Song, S. Song, W. Zhang, H. Han, K. Wei, D. Liu, Q. Wang, C. Ma and S. Feng, *Fuel*, 2024, **366**, 131154.
43 W. Chen, B. Han, Y. Xie, S. Liang, H. Deng and Z. Lin, *Chem. Eng. J.*, 2020, **391**, 123519.
44 C. Liu, W. Wang, M. Zhang, C. Zhang, C. Ma, L. Cao, D. Kong, H. Feng, W. Li and S. Chen, *Chem. Eng. J.*, 2022, **430**, 132663.
45 W. Wang, C. Liu, M. Zhang, C. Zhang, L. Cao, C. Zhang, T. Liu, D. Kong, W. Li and S. Chen, *J. Colloid Interface Sci.*, 2022, **608**, 735–748.
46 J. Li, Z. Yang, C. Wang, S. Wu, Y. Zheng, Z. Cui, H. Jiang, Z. Li, S. Zhu, L. Feng and X. Liu, *Appl. Catal., B*, 2023, **339**, 123163.
47 M. Ronda-Lloret, T. K. Slot, N. P. van Leest, B. de Bruin, W. G. Sloof, E. Batyrev, A. Sepúlveda-Escribano, E. V. Ramos-Fernandez, G. Rothenberg and N. R. Shiju, *ChemCatChem*, 2022, **14**(18), e202200446.
48 W. Jeitschko, H. T. Nowotny and F. Benesovsky, *J. Less-Common Met.*, 1964, **7**(2), 133.
49 T. K. Slot, P. Oulego, Z. Sofer, Y. Bai, G. Rothenberg and N. R. Shiju, *ChemCatChem*, 2021, **13**(15), 3470.
50 J. A. Kumar, P. Prakash, T. Krithiga, D. J. Amarnath, J. Premkumar, N. Rajamohan, Y. Vasseghian, P. Saravanan and M. Rajasimman, *Chemosphere*, 2022, **286**, 131607.
51 K. Chaturvedi, V. Hada, S. Paul, B. Sarma, D. Malvi, M. Dhangar, H. Bajpai, A. Singhwane, A. K. Srivastava and S. Verma, *Top. Curr. Chem.*, 2023, **381**(2), 11.
52 Y. Qu, C. Shi, H. Cao and Y. Wang, *Mater. Lett.*, 2020, **280**, 128526.
53 I. Amin, H. V. D. Brekel, K. Nemani, E. Batyrev, A. de Vooys, H. van der Weijde, B. Anasori and N. R. Shiju, *ACS Appl. Mater. Interfaces*, 2022, **14**(38), 43749–43758.
54 M. Benchakar, L. Loupias, C. Garnero, T. Bilyk, C. Morais, C. Canaff, N. Guignard, S. Morisset, H. Pazniak, S. Hurand, P. Chatier, J. Pacaud, V. Mauchamp, M. W. Barsoum, A. Habrioux and S. Celerier, *Appl. Surf. Sci.*, 2020, **530**, 147209.
55 D. Dolz, A. Morales-García, F. Viñes and F. Illas, *Nanomaterials*, 2012, **11**(1), 127.
56 C. Zhang and M. Naguib, *Transition Metal Carbides and Nitrides (MXenes) Handbook: Synthesis, Processing, Properties and Applications*, John Wiley & Sons, 2024.
57 H. Lashgari, M. R. Abolhassani, A. Boochani, S. M. Elahi and J. Khodadadi, *Solid State Commun.*, 2014, **195**, 61.
58 G. R. Berdiyorov, *AIP Adv.*, 2016, **6**(5), 055105.
59 P. Verma, U. P. Singh, R. J. Butcher, S. Banerjee and P. Roy, *J. Mol. Struct.*, 2022, **1249**, 131590.
60 U. P. Singh, P. Verma and R. J. Butcher, *J. Mol. Struct.*, 2021, **1224**, 129161.
61 M. O'Keeffe and O. M. Yaghi, *Chem. Rev.*, 2012, **112**(2), 675.
62 M. Treger, A. Hannebauer, A. Schaate, J. L. Budde, P. Behrens and A. M. Schneider, *Phys. Chem. Chem. Phys.*, 2023, **25**(8), 6333–6341.
63 X. Qiu, Y. Zhu, X. Zhang, Y. Zhang, L. T. Menisa, C. Xia, S. Liu and Z. Tang, *Solar RRL*, 2020, **4**(8), 1900449.
64 C. K. Lin, D. Zhao, W. Y. Gao, Z. Yang, J. Ye, T. Xu, Q. Ge, S. Ma and D.-J. Liu, *Inorg. Chem.*, 2012, **51**(16), 9039.
65 J. Gascon, M. D. Hernández-Alonso, A. R. Almeida, G. P. van Klink, F. Kapteijn and G. Mul, *ChemSusChem*, 2008, **1**(12), 981.
66 X. Ma, L. Wang, Q. Zhang and H.-L. Jiang, *Angew. Chem.*, 2019, **131**, 12303.
67 Z. Qian, R. Zhang, H. Hu, Y. Xiao, H. Li, X. Sun and T. Ma, *Sol. RRL*, 2023, **7**, 2300547.
68 A. Jamma, B. Jaksani, C. S. Vennapoosa, S. Gonuguntla, S. Sk, M. Ahmadipour, M. Abraham B, I. Mondal and U. Pal, *Mater. Adv.*, 2024, **5**(7), 2785.
69 S. Sk, A. Jamma, D. S. Gavali, V. Bhasin, R. Ghosh, K. Sudarshan, R. Thapa and U. Pal, *ACS Appl. Mater. Interfaces*, 2023, **15**, 55822.
70 S. Navalón, A. Dhakshinamoorthy, M. Álvaro, B. Ferrer and H. García, *Chem. Rev.*, 2022, **123**(1), 445–490.
71 X. Tan, J. Zhang, J. Shi, X. Cheng, D. Tan, B. Zhang, L. Liu, F. Zhang, B. Han and L. Zheng, *Sustainable Energy Fuels*, 2020, **4**(6), 2823–2830.
72 A. Maleki and R. Taheri-Ledari, *Physicochemical Aspects of Metal-Organic Frameworks: A New Class of Coordinative Materials*, Springer Nature, 2023.
73 M. Dan-Hardi, C. Serre, T. Frot, L. Rozes, G. Maurin, C. Sanchez and G. Férey, *J. Am. Chem. Soc.*, 2009, **131**(31), 10857–10859.
74 T. Davide, F. Marc, S. Clément, S. Capucine, R. Laurence, M. D. Caroline and W. Aron, *J. Am. Chem. Soc.*, 2013, **135**, 10942.
75 M. Sohail, S. Rauf, M. Irfan, A. Hayat, M. M. Alghamdi, A. A. El-Zahhar, D. L. Ghernaout, Y. Al-Hadeethi and W. Lv, *Nanoscale Adv.*, 2024, **6**(5), 1286–1330.
76 H. Q. Pham, T. Mai, N. N. Pham-Tran, Y. Kawazoe, H. Mizuseki and D. Nguyen-Manh, *J. Phys. Chem. C*, 2014, **118**(9), 4567–4577.
77 J. Patel, G. Bury and Y. Pushkar, *Small*, 2024, 2310106.
78 K. Geng, T. He, R. Liu, S. Dalapati, K. T. Tan, Z. Li, S. Tao, Y. Gong, Q. Jiang and D. Jiang, *Chem. Rev.*, 2020, **120**(16), 8814.
79 A. P. Cote, A. I. Benin, N. W. Ockwig, M. O'Keeffe, A. J. Matzger and O. M. Yaghi, *Science*, 2005, **310**(5751), 1166.
80 S. Patial, V. Soni, A. Kumar, P. Raizada, T. Ahamad, X. M. Pham, Q. V. Le, V.-H. Nguyen, S. Thakur and P. Singh, *Environ. Res.*, 2023, **218**, 114982.
81 H. Wang, H. Wang, Z. Wang, L. Tang, G. Zeng, P. Xu, M. Chem, T. Xiong, C. Zhou, X. Li, D. Huang, Y. Zhu, Z. Wang and J. Tang, *Chem. Soc. Rev.*, 2020, **49**(12), 4135–4165.
82 M. Li, C. Gong, J. Du, D. Ding, D. Du, D. Wang, J. Jiang, T. Li, C. Zhang, Y.-F. Yang, Y. She and J. Jia, *ACS Mater. Lett.*, 2023, **5**(3), 694.
83 P. Pachfule, A. Acharjya, J. Roeser, T. Langenhahn, M. Schwarze, R. Schomäcker, A. Thomas and J. Schmidt, *J. Am. Chem. Soc.*, 2018, **140**(4), 1423.
84 Y. Chen, X. Luo, J. Zhang, L. Hu, T. Xu, W. Li, L. Chen, M. Shen, S.-B. Ren, D.-M. Han, G.-H. Ning and D. Li, *J. Mater. Chem. A*, 2022, **10**(46), 24620.
85 L. Yin, Y. Zhao, Y. Xing, H. Tan, Z. Lang, W. Ho, Y. Wang and Y. Li, *Chem. Eng. J.*, 2021, **419**, 129984.
86 X. Pei, P. He, K. Yu, Y. Li, Y. Tang and L. Ma, *Adv. Funct. Mater.*, 2024, 2410827.
87 W. Wang, D. Huang, W. Zheng, X. Zhao, K. He, H. Pang and Y. Xiang, *Chem. Mater.*, 2023, **35**(17), 7154.
88 R. Freund, O. Zaremba, G. Arnauts, R. Ameloot, G. Skorupskii, M. Dincă, A. Bavykina, J. Gascon, A. Ejsmont, J. Goscianska, M. Kalmutzki, U. Lachelt, E. Ploetz, C. S. Diercks and S. Wuttke, *Angew. Chem., Int. Ed.*, 2021, **60**(45), 23975.
89 F. Ahmadijokani, A. Ghaffarkhah, H. Molavi, S. Dutta, Y. Lu, S. Wuttke, M. Kamkar, O. J. Rojas and M. Arjmand, *Adv. Funct. Mater.*, 2023, 2305527.

90 N. H. Solangi, R. R. Karri, S. A. Mazari, N. M. Mubarak, A. S. Jatoi, G. Malafaia and A. K. Azad, *Coord. Chem. Rev.*, 2023, **477**, 214965.
91 Q. Zhong, Y. Li and G. Zhang, *Chem. Eng. J.*, 2021, **409**, 128099.
92 S. Kashif, S. Akram, M. Murtaza, A. Amjad, S. S. A. Shah and A. Waseem, *Diamond Relat. Mater.*, 2023, **136**, 110023.
93 K. Nabeela, R. Deka, Z. Abbas, P. Kumar, M. Saraf and S. M. Mobin, *Cryst. Growth Des.*, 2023, **23**(5), 3057.
94 Y. Wen, Z. Wei, C. Ma, X. Xing, Z. Li and D. Luo, *Nanomaterials*, 2019, **9**(5), 775.
95 Q. Geng, H. Wang, Y. Wu, L. P. Lv, S. Chen, W. Sun and Y. Wang, *ChemElectroChem*, 2022, **9**(16), e202200340.
96 Y. Zhao, K. Hu, C. Yang, X. Liu, L. Li, Z. Li, P. Wang, Z. Zhang and S. Zhang, *Anal. Chim. Acta*, 2023, **1237**, 340581.
97 X. Gong, G. Zhang, H. Dong, H. Wang, J. Nie and G. Ma, *J. Membr. Sci.*, 2022, **657**, 120667.
98 C. Wei, Y. Wang, Y. Zhang, L. Tan, Y. Qian, Y. Tao, S. Xiong and J. Feng, *Nano Res.*, 2021, **14**, 3576.
99 H. Wang, R. Zhao, J. Qin, H. Hu, X. Fan, X. Cao and D. Wang, *ACS Appl. Mater. Interfaces*, 2019, **11**(47), 44249.
100 Y. Liu, Y. He, E. Vargun, T. Plachy, P. Saha and Q. Cheng, *Nanomaterials*, 2020, **10**(4), 695.
101 Y. Sun, M. Xie, H. Feng and H. Liu, *ChemPlusChem*, 2022, **87**(4), e202100553.
102 T. Xiao, J. Jin, Y. Zhang, W. Xi, R. Wang, Y. Gong, B. He and H. Wang, *Electrochim. Acta*, 2022, **427**, 140851.
103 Y. Wang, J. Song and W. Y. Wong, *Angew. Chem.*, 2023, **135**(8), e202218343.
104 X. Zhao, H. Xu, Z. Hui, Y. Sun, C. Yu, J. Xue, R. Zhou, L. Wang, H. Dai, Y. Zhao, J. Yang, J. Zhou, Q. Chen and W. Huang, *Small*, 2019, **15**(47), 1904255.
105 A. Wei, L. Wang and Z. Li, *J. Alloys Compd.*, 2022, **899**, 163369.
106 C. Ruan, D. Zhu, J. Qi, Q. Meng, F. Wei, Y. Ren, Y. Sui and H. Zhang, *Surf. Interfaces*, 2021, **25**, 101274.
107 X. Zhang, S. Yang, W. Lu, D. Lei, Y. Tian, M. Guo, P. Mi, N. Qu and Y. Zhao, *J. Colloid Interface Sci.*, 2021, **592**, 95.
108 Y. Yang, X. Huang, C. Sheng, Y. Pan, Y. Huang and X. Wang, *J. Alloys Compd.*, 2022, **920**, 165908.
109 B. P. Mishra, L. Biswal, S. Das, L. Acharya and K. Parida, *Langmuir*, 2023, **39**(3), 957.
110 H. Gu, H. Zhang, X. Wang, Q. Li, S. Chang, Y. Huang, L. Gao, Y. Cui, R. Liu and W.-L. Dai, *Appl. Catal., B*, 2023, **328**, 122537.
111 L. Cheng, Y. Tang, M. Xie, Y. Sun and H. Liu, *J. Alloys Compd.*, 2021, **864**, 158913.
112 S. G. Nnabuife, J. Ugbeh-Johnson, N. E. Okeke and C. Ogbonnaya, *Carbon Capture Sci. Technol.*, 2022, **3**, 100042.
113 M. M. Ayyub, M. Chhetri, U. Gupta, A. Roy and C. N. R. Rao, *Chem. – Eur. J.*, 2018, **24**(69), 18455.
114 T. Ohta, *Int. J. Hydrogen Energy*, 1988, **13**(6), 333–339.
115 L. Zhao, B. Dong, S. Li, L. Zhou, L. Lai, Z. Wang, S. Zhao, M. Han, K. Gao, M. Lu, X. Xie, B. Chen, Z. Liu, X. Wang, H. Zhang, H. Li, J. Liu, H. Zhang, X. Huang and W. Huang, *ACS Nano*, 2017, **11**(6), 5800.
116 D. Chen, Y. Cheng, N. Zhou, P. Chen, Y. Wang, K. Li, S. Huo, P. Cheng, P. Peng, R. Zhang, L. Wang, H. Liu, Y. Liu and R. Ruan, *J. Cleaner Prod.*, 2020, **268**, 121725.
117 N. M. Mahmoodi, *J. Mol. Catal. A: Chem.*, 2013, **366**, 254.
118 E. Issaka, J. N. O. Amu-Darko, S. Yakubu, F. O. Fapohunda, N. Ali and M. Bilal, *Chemosphere*, 2022, **289**, 133208.
119 O. Tavakoli, V. Goodarzi, M. R. Saeb, N. M. Mahmoodi and R. Borja, *J. Hazard. Mater.*, 2017, **334**, 256.
120 H. Assad, I. Fatma, A. Kumar, S. Kaya, D. V. N. Vo, A. Al-Gheethi and A. Sharma, *Chemosphere*, 2022, **298**, 134221.
121 N. Nasrollahi, S. Aber, V. Vatanpour and N. M. Mahmoodi, *Composites, Part B*, 2018, **154**, 388.
122 W. Zhou, P. Wu, L. Zhang, D. Zhu, X. Zhao and Y. Cai, *J. Hazard. Mater.*, 2022, **421**, 126721.
123 X. Li, Y. Pi, Q. Hou, H. Yu, Z. Li, Y. Li and J. Xiao, *Chem. Commun.*, 2018, **54**(15), 1917.
124 E. Erdural, U. Bolukbasi and G. Karakas, *J. Photochem. Photobiol., A*, 2014, **283**, 29.
125 O. Bechambi, M. Chalbi, W. Najjar and S. Sayadi, *Appl. Surf. Sci.*, 2015, **347**, 414.
126 K. Dulta, G. Koşarsoy Ağçeli, P. Chauhan, R. Jasrotia, P. K. Chauhan and J. O. Ighalo, *Sustainable Environ. Res.*, 2022, **32**, 1.
127 M. Zhang, K. Wang, S. Zeng, Y. Xu, W. Nie, P. Chen and Y. Zhou, *Chem. Eng. J.*, 2021, **411**, 128517.